FAR-INFRARED STUDIES OF EXCITONS IN GERMANIUM AND SILICON

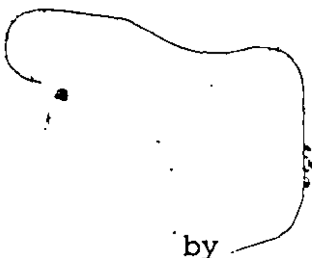

by

© DANIEL LABRIE

A Thesis
Submitted to the School of Graduate Studies
in Partial Fulfilment of the Requirements
for the Degree
Doctor of Philosophy

McMaster University
August, 1984

FAR-INFRARED STUDIES OF EXCITONS IN GERMANIUM AND SILICON

DOCTOR OF PHILOSOPHY (1984)
(Physics)

McMASTER UNIVERSITY
Hamilton, Ontario

TITLE: Far-Infrared Studies of Excitons in Germanium and Silicon

AUTHOR: Daniel Labrie, B.Sc. (Université de Montréal)
M.Sc. (McMaster University)

SUPERVISOR: Dr. T. Timusk

NUMBER OF PAGES: xi, 88

ABSTRACT

This thesis examines three aspects of exciton physics by using far-infrared (FIR) spectroscopy. First, the energy level structure of free excitons was investigated in germanium under the application of a uniaxial, compressive stress along the [111] direction. At high stress, the exciton absorption spectra display a nearly hydrogenic-like structure with strong, isolated absorption lines. A theoretical model was developed to predict the positions and strengths of these absorption lines. Excellent agreement was obtained between experiment and theory. This is in contrast to the situation at zero stress where the exciton spectrum is not understood very well.

Then, the first measurement of the FIR absorption spectrum of a bound exciton is reported. This spectrum provides information on the odd parity excited states of the bound exciton which cannot be observed using conventional near-infrared spectroscopy. The bound exciton absorption spectrum was found to be in excellent agreement with those of acceptors in silicon, giving the best confirmation of the model of the energy level structure of an isoelectronic bound exciton.

Finally, the thermodynamic equilibrium between free excitons and carriers is investigated in germanium. Their absolute concentrations were obtained from their FIR

absorptions. Measurements of the exciton and carrier concentrations allowed a direct determination of the equilibrium constant for any given temperature and carrier generation rate. The experimental equilibrium constant was found to be in excellent agreement with the classical equilibrium constant of an ideal gas.

ACKNOWLEDGEMENTS

I would sincerely like to thank my supervisor, Dr. Tom Timusk, for his guidance, good humour, and most importantly, for his lasting effort in helping me become a better physicist. I am very grateful to Dr. Mike Thewalt for the idea that started the study of bound excitons, for his continual interest and many fruitful discussions throughout this project. I am indebted to Dr. Dave Goodings for several helpful discussions on the theoretical aspect of the free exciton level structure in stressed germanium.

I would particularly like to thank Mr. Jim Garrett and Mr. Clarence Verge, for their availability and generous help in building the stress sensor and other things. Thanks to my colleague, Mr. Rick Scholes, with whom I had fruitful and enjoyable conversations, and for his help in calibrating the stress sensor. Thanks also to Mr. Andy Duncan, and to others in and around the lab, for countless odd jobs and one-liners.

I thank Drs. Eugene E. Haller, W.L. Hansen and Ed Lightowlers for generously supplying the high quality Ge samples and the Be-doped Si samples. Thanks to Dr. Graciela Zárate, for providing a copy of her program to evaluate the dielectric constant and for several helpful discussions related to her work.

I am grateful to Ms. Helen Kennelly and Ms. Erie Long for their rapid and accurate typing of this thesis and to Messrs. Rob Klassen, Doug Bonn, Hon Kie Ng, and Paul Laroche who have made this thesis more readable.

This work was supported, in part, by McMaster University, the Natural Sciences and Engineering Research Council of Canada and the Ontario Graduate Scholarship.

Finalement, je voudrais témoigner ma gratitude à mes parents, Jeanette et Roger Labrie, pour leur support moral et spirituel durant toute ses années.

TABLE OF CONTENTS

		Page
CHAPTER 1	INTRODUCTION	1
CHAPTER 2	EXPERIMENTAL TECHNIQUES	6
	2.1 Introduction	6
	2.2 Sample Preparation	8
	2.3 Far Infrared Sources, Detector and Optical Techniques	9
	2.4 Cryogenic Techniques and Data Collection	11
	2.5 Stress System and Calibration	14
CHAPTER 3	FAR-INFRARED ABSORPTION SPECTRUM OF EXCITONS IN [111]-STRESSED GERMANIUM: HIGH STRESS LIMIT	22
	3.1 Introduction	22
	3.2 Band Structure of Germanium	24
	3.3 Theoretical Model for the Energy Levels of Excitons in [111]-Stressed Germanium	29
	3.4 Experimental Results and Discussion	36
CHAPTER 4	FAR-INFRARED ABSORPTION SPECTRUM OF Be-RELATED BOUND EXCITONS IN SILICON	42
	4.1 Introduction	42
	4.2 Hopfield, Thomas and Lynch Model of an Isoelectronic Bound Exciton	43
	4.3 Experimental Results and Discussion	46
CHAPTER 5	DIRECT DETERMINATION OF THE EQUILIBRIUM CONSTANT OF THE EXCITON-CARRIER GAS IN GERMANIUM	57
	5.1 Introduction	57

Page

5.2 Far-Infrared Absorption Spectrum of Free Carriers in Germanium 59

5.3 Thermodynamics of Exciton-Carrier Gas in Germanium 66

CHAPTER 6 CONCLUSIONS 76

APPENDIX A EVALUATION OF THE ENERGY LEVELS OF EXCITONS 79

BIBLIOGRAPHY 82

LIST OF FIGURES

		Page
Fig. 2-1	Schematic diagram of the apparatus used for the investigation of the exciton gas in germanium and silicon.	7
Fig. 2-2	Schematic diagram of the assembly used in the experiments.	12
Fig. 2-3	Cross-sectional detail of the probe sample holder, showing part of the stress system.	15
Fig. 2-4	Circuit diagram of the oscillator employed with the stress sensor to calibrate the stress system.	17
Fig. 2-5	Cut-away schematic drawing of stress system with stress sensor.	19
Fig. 3-1	Calculated energy band structure of Ge for two directions of wavevector $\underline{k}$.	25
Fig. 3-2	Band structures of Ge as a function of stress.	28
Fig. 3-3	Calculated 1S, $2P_0$ and $2P_\pm$ energy levels as a function of the reduced mass ratio, $\gamma = \mu_t/\mu_l$, of exciton in the high stress limit.	34
Fig. 3-4	Far-infrared absorption spectra of excitons in Ge as a function of uniaxial [111] stress.	37
Fig. 3-5	Plot of the exciton line positions as a function of the reciprocal stress 1/S.	39
Fig. 4-1	Schematic energy level diagram of the ground states of an IBE under a series of interactions.	45
Fig. 4-2	Uncorrected FIR transmission spectrum of Be-doped Si sample without laser illumination (top), and induced FIR absorption when a Kr^+ laser was incident on the sample (bottom).	47

Page

Fig. 4-3	Temperature dependence of the induced absorption spectrum.	49
Fig. 4-4	Comparison of transitions determined by NIR and FIR spectroscopy.	51
Fig. 4-5	Comparison between the even parity excited states of boron acceptor with those of IBE.	55
Fig. 5-1	Theoretical FIR absorption spectrum of free carriers.	62
Fig. 5-2	Theoretical intraband contribution to the free carrier absorption coefficient at several values of the Drude damping constant.	64
Fig. 5-3	Calculated interband contribution to the free carrier absorption coefficient at 6.5 K, 12 K, and 34 K.	65
Fig. 5-4	Temperature dependence of the absorption of free carriers and excitons at constant laser power.	67
Fig. 5-5	Decomposition of the total absorption into free carrier and exciton absorptions.	70
Fig. 5-6	High temperature absorption spectrum of excitons and free carriers.	72
Fig. 5-7	Thermodynamic equilibrium constant as a function of temperature.	73

LIST OF TABLES

		Page
Table 3-1	Band structure parameters for Ge.	27
Table 3-2	Variational wavefunctions for the low-lying levels of excitons.	33
Table 3-3	Experimental and theoretical line positions of excitons in the high stress limit.	40
Table 4-1	Comparison of energy level differences as determined by NIR and FIR spectra.	52

CHAPTER 1

INTRODUCTION

Many of the fundamental optical properties of insulators are due to electronic states located below the lowest conduction band. These low-lying states, called excitons, were first observed by Hilsch and Pohl [1] who investigated the near absorption edge of alkali halides. It was several years later than Frenkel, Peierls, Wannier and Mott [2-6] developed a theory of excitons.

Frenkel studied the specific case of an electronic excitation of a lattice atom. Due to the translational symmetry of the lattice, the excitation is not localized at a given atom but travels within the crystal. The Frenkel exciton can be visualized as an electrostatically bound electron and hole where both particles lie on a single atom. It is observed in solid inert gases which have low carrier mobilities and dielectric constants. The exciton binding energy in these crystals is typically ~ 1 eV which reflects the spatial localization of the electron and hole.

Wannier and Mott considered the case of an exciton composed of an electron in the lowest conduction band and a hole in the upper valence band. These excitons can be regarded as particles in a homogeneous medium where the physical properties of the crystal are expressed in terms of

the electron and hole effective masses and the static dielectric constant. The Wannier-Mott excitons are observed in predominantly covalent crystals (such as: germanium, cadmium sulfide and cuprous oxide) which have high carrier mobilities and dielectric constants. Their energy level structure is analogous to that of a hydrogen atom and is characterized by a Rydberg energy and a Bohr radius:

$$E_{ex} = \frac{m^*}{m_e} \frac{1}{\varepsilon^2} E_I \,, \tag{1-1}$$

$$a_{ex} = \frac{m_e}{m^*} \varepsilon \, a_0 \,. \tag{1-2}$$

The binding energy and Bohr radius of the hydrogen atom are given by E_I and a_0, respectively, where m_e is the free electron mass, m^* is the reduced mass of the electron and hole, and ε is the static dielectric constant of the crystal. The large dielectric constant (ε>10) and small reduced mass (m^*<0.1 m_e) in typical semiconductors result in a Rydberg energy $E_{ex} \sim 10^{-2}$ eV and Bohr radius $a_{ex} \sim 10^2$ Å. This high value of a_{ex} indicates that the wavefunction of a Wannier-Mott exciton is delocalized over many lattice constants.

Excitons in intrinsic semiconductors can be produced in high concentrations by using band gap light excitation at low temperatures. Under these conditions electrons from the valence band are excited across the gap to the conduction band leaving behind holes in the valence band. The generated

electrons and holes relax nonradiatively (via phonon emission) to the minimum of the conduction band and the maximum of the valence band, respectively. At sufficiently low temperatures, free carriers bind together to form excitons. The resulting population of free carriers and excitons is in quasi-thermal equilibrium with the crystal lattice since the carriers' and excitons' lifetimes ($\sim 10^{-6}$ sec) are much longer than the typical collision time with the lattice ($\sim 10^{-9}$ sec). This thermal equilibrium is manifested (under suitable conditions) by a chemical equilibrium between free carriers and excitons, similar to that of H_2O and its chemical constituents.

Excitons bound to impurities can also occur in doped semiconductors. The first evidence of bound excitons (BE) was obtained by Haynes [7]. He observed sharp additional photoluminescence lines in silicon containing low concentrations of donors and acceptors. Their narrow linewidths as compared to those of free excitons indicated that BE do not have any kinetic energy. Haynes also suggested that the binding mechanism of an exciton trapped by an acceptor is due to a hole pair bond tying together the electron and the negative ion acceptor. The reverse is true for an exciton bound to a donor. Excitons can also be bound to isoelectronic traps. Unlike donors and acceptors, these traps satisfy the four neighbouring bonds of the lattice site and they do not have any excess charges present. They bind a

primary particle, either an electron or a hole through their short range potential. The secondary particle is then bound by the long range coulomb potential of the primary one. These traps can change the structure of a bound exciton into two possible alternatives. For a weak short range potential of the impurity centre, the bound exciton quantum structure will be that of a perturbed exciton with an ionization energy close to the free exciton binding energy. In the case of a strong short range potential, the primary particle will be localized near the trap and the secondary particle will then have an excited state spectrum similar to that of a donor or an acceptor.

The aim of this thesis is to study three aspects of exciton physics. The first part of this thesis consists of investigating the energy level structure of free excitons in [111]-stressed germanium. A series of experiments was performed to measure the far-infrared (FIR) absorption spectrum of excitons in stressed Ge with the stress axis along the [111] direction. The line positions of the 1S-2P and 1S-3P transitions and the relative absorption associated with the 1S-2P transitions were found to be in good agreement with a simple theoretical model. The model only considers the lower conduction band minima and the upper valence band maxima at high stress in the formation of excitons.

In the second part of this thesis, the first measurement of the FIR absorption spectrum of an exciton

bound to an isoelectronic trap is reported. The spectrum provides information on transitions from the even parity ground states to the odd parity excited states. The excited state spectrum of the bound exciton was found to be in excellent agreement with the spectra of acceptors in Si. This shows that FIR spectroscopy applied to the study of bound excitons reveals without ambiguity the nature of the bound exciton.

In the last part of this thesis, the thermodynamic equilibrium between free carriers and excitons is examined using FIR spectroscopy. Their absolute concentrations were obtained from the FIR absorption associated with free carriers and excitons respectively. Measurements of their concentrations at several temperatures demonstrated that free carriers and excitons behave like ideal gases in thermal equilibrium with each other.

Chapter 2 describes the experimental apparatus and techniques used to measure the FIR absorption associated with free and bound excitons, and free carriers. Chapters 3 and 4 present the results on the investigation of the energy level structure of free excitons in stressed germanium and bound excitons in doped silicon, respectively. Chapter 5 is concerned with the study of the thermodynamic equilibrium of the exciton-carrier gas in germanium. Finally, Chapter 6 summarizes the results and conclusions of these studies.

CHAPTER 2

EXPERIMENTAL TECHNIQUES

2.1 Introduction

The general form of the apparatus used in the experiments is illustrated schematically in Fig. 2-1. The excitons were generated via band gap light excitation. A (Sylvana) CW YAG:Nd laser operating at a wavelength of 1.06 μm and with incident power at the sample from 10 to 20 mW was employed in germanium while a krypton laser (Spectra-Physics) operating at a wavelength of 0.65 μm and with incident power of 60 mW was used in silicon. The FIR radiation is provided by an interferometer. Both the laser and FIR beam are directed onto the sample. The near infrared beam is absorbed within a few microns at the surface of the sample while the FIR beam is weakly absorbed by the generated exciton gas. The transmitted FIR radiation is received by a detector whose output is processed by a computer to provide the relative transmitted intensity and the absorptance as a function of frequencies. The experiments were conducted in the temperature range from 1.2 K to 34 K. The absorptance by excitons αd was derived from the following formula

$$\alpha d = \ell n(I_0/I) \quad . \tag{2-1}$$

Fig. 2-1

Schematic diagram of the apparatus utilized for the investigation of the exciton gas in germanium and silicon.

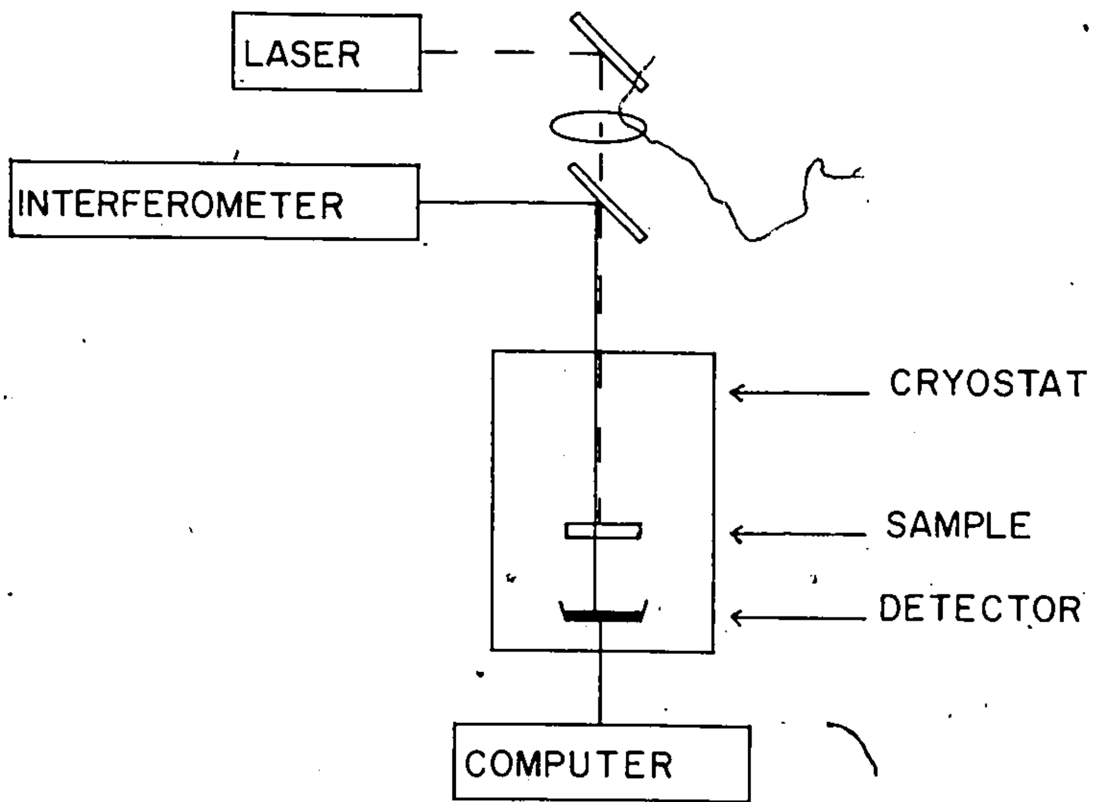
LASER
INTERFEROMETER
CRYOSTAT
SAMPLE
DETECTOR
COMPUTER

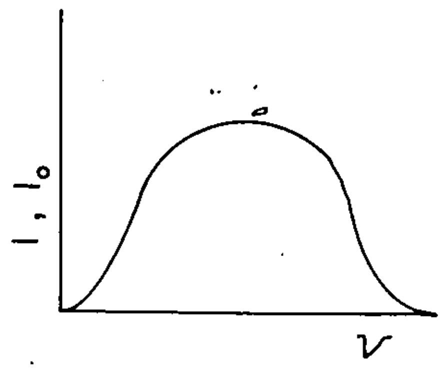
I, I₀
ν

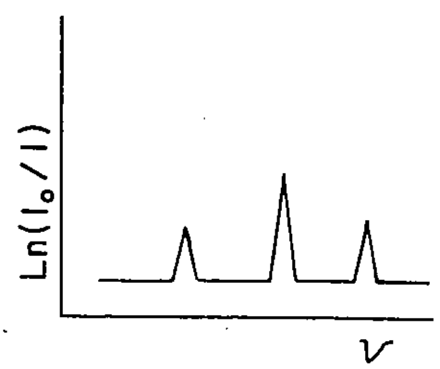
Ln(I₀/I)
ν

$I_0(\omega)$ represents the transmitted FIR radiation through the sample when there were no excitons present, i.e. when the laser was off and $I(\omega)$ is the transmitted radiation when excitons were generated, i.e. when the laser was on. d is the absorption length by excitons. Typical figures for the measured absorptance in germanium and silicon varied between 0.1 and 0.8.

2.2 Sample Preparation

The Ge samples employed in the experiments were grown by Haller and Hansen [8]. The samples were cut from dislocation-free Ge crystals with a concentration of electrically active impurities $(N_A-N_D) \leq 2\times10^{11}$ cm^{-3} where N_A and N_D are the concentrations of acceptors and donors respectively. In the stress experiments, a crystal was first oriented to within 0.5° by using the Laue method and cut with a diamond grit wafering blade along the [111], [11$\bar{2}$], and [1$\bar{1}$0] directions. The resulting sample was mechanically polished with silicon carbide paper and with 6 μm and 1 μm diamond paste. The sample was then etched in CP4A solutions (HNO_3, HF, CH_3COOH; 5:3:3) to reduce surface recombination. The crystal obtained was of dimensions 7.67×1.52×2.17 mm^3. The [11$\bar{2}$] face was wedged with an angle of 1.8° to remove any spurious reflections. The longest dimension was along the [111] direction. The [111] surfaces were not etched to avoid surface irregularities and, hence, stress inhomogeneities.

The Ge sample used to study the thermodynamic equilibrium between free carriers and excitons was a wafer with a diameter of 3.4 cm and with a thickness of 0.6 mm. The largest face was along the [113] direction. The sample was etched in CP4A solution to remove any damages produced by the saw. The final sample thickness was 0.37 mm.

The Be-doped silicon sample was provided by E.C. Lightowlers [9]. The crystal was of dimensions $2.80\times1.0\times10.74\ mm^3$. The doping technique mainly consisted of evaporating a film of Be onto several 2 mm thick wafers of zone-refined Si (Hoboken 20 kΩ.cm). The wafers were stacked in pairs with the coated sides adjacent to each other and heated to ∿ 1000°C for about an hour. At this temperature the Beryllium diffuses into the bulk of the wafers. The doping procedure is described in detail by Crouch et al. [10].

2.3 Far Infrared Sources, Detector and Optical Techniques

The FIR radiation was provided by two Fourier transform spectrometers. A custom built (C. Zarate) Martin-Puplett type Michelson interferometer [11] was utilized in the spectral range from 1 meV to 19 meV. The input polarizer, beam splitter and output analyser were wire grid polarizers (Analytical Accessories Ltd.) with a wire diameter of 5 μm and with a spacing g between the wires of 9.5 μm. The analyser was rotated at a frequency of 35 Hz. The moving mirror was driven by a Slo-Syn HS25V stepping motor.

The advantage of this type of interferometer over a conventional Michelson interferometer is that the wire grid beam splitter is nearly 100% efficient at low wavevector while the Mylar beam splitter of a Michelson interferometer decreases to zero as the wavevector squared. However the available spectral range of a Martin-Puplett type interferometer is limited by the efficiency of the polarizers at high frequencies. The cutoff frequency of the interferometer is roughly $\sim 1/2g \sim 500\ cm^{-1}$.

In the spectral range from 10 meV to 40 meV, a commercial Michelson interferometer (RIIC FS 720) was employed with a 6 μm thick (25G) Mylar beam splitter. The original mirror drive system was replaced by a hydrostatic pumped-oil bearing for rapid scanning operation [12]. This new drive provided a smooth, regular and very accurate motion of the moving mirror. The light source used in the Martin-Puplett type Michelson interferometer was a mercury arc in a fused quartz envelope (American Ultraviolet MPQ/400) while a DVY (GTE Sylvania) tungsten halogen lamp was utilized in the Michelson interferometer. The detector employed to detect the transmitted radiation was a composite germanium bolometer [13] operating at 0.3 K.

To restrict the spectral range of the incoming radiation several band pass filters were used. The first one had a cutoff of 33 cm^{-1} and was made from aluminium capacitive grids deposited on black polyethylene [14]. A

125 cm^{-1} cutoff filter was made from a suspension of KBr, NaCl and NaF powders in polyethylene [15] together with 0.004" thick black polyethylene. The 200 cm^{-1} cutoff filter was obtained from a wedged NaF crystal in combination with 0.003" thick black polyethylene and a 400 cm^{-1} cutoff filter was formed from a sapphire plate coated with a film of carbon soot.

2.4 Cryogenic Techniques and Data Collection

A schematic diagram of the assembly used in the experiments is shown in Fig. 2-2. The assembly consisted of a "probe" and an "insert". The main purpose of the probe was to guide the FIR radiation from the interferometer to the sample, and from the sample to the detector. The insert provided a ^{3}He cryostat housing for the detector and allowed the experiments to be done in superfluid ^{4}He or in exchange gas. A detailed description of the insert including some design considerations is given by H. Navarro [17].

The probe shown in Fig. 2-2 was used in the stress experiments. FIR radiation from the interferometer was directed at the entrance of a 0.0005" thick Mylar window. The transmitted FIR beam was reflected down the light pipe by a polished brass plate which had a small glass window for the incoming laser beam. The laser beam was focused by an external lens to a 2 mm diameter spot at the sample surface while the FIR beam was focused by a condensing cone to the same spot diameter at the sample. A 1000 lines/inch

Fig. 2-2

Schematic diagram of the assembly used in the experiments. The assembly was inserted into a ^{4}He cryostat. The Mylar window transmitted the FIR radiation while the glass window admitted the near infrared laser beam. A brass cap covered the sample to eliminate any stray radiation and held the filter in place. When required, a ^{4}He inlet valve was operated from outside the cryostat to let the ^{4}He liquid into the sample chamber. The detector chamber, located below the sample, thermally isolated the detector from the rest of the assembly such that it could be continuously operated at 0.33 K via a ^{3}He cooling system. The system was composed of a ^{3}He storage can, an adsorption charcoal pump, and a ^{3}He can. The detector temperature was monitored with a calibrated carbon resistor. (Figure taken from Scholes [16]).

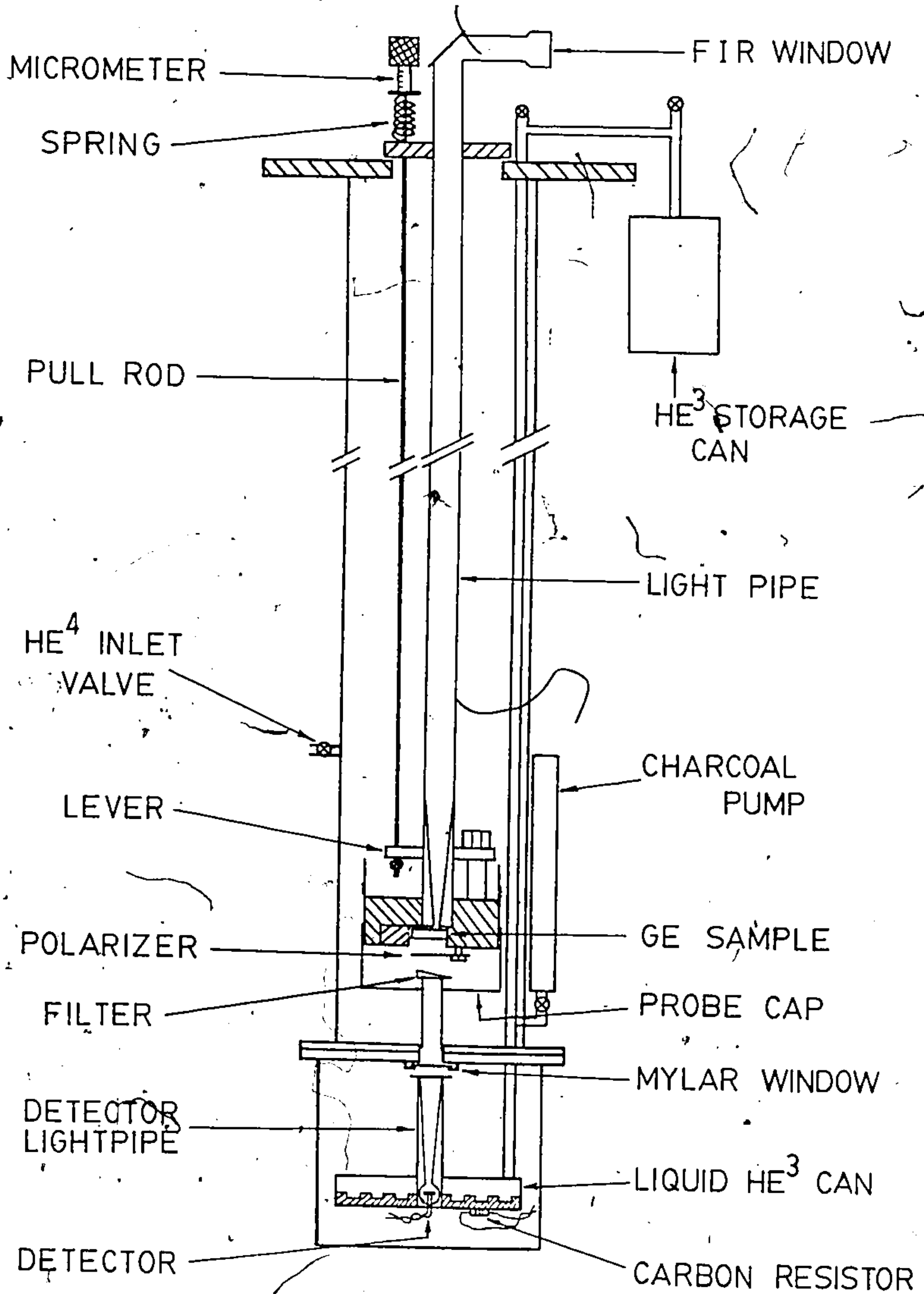
FIR WINDOW
MICROMETER
SPRING
PULL ROD
HE3 STORAGE CAN
LIGHT PIPE
HE4 INLET VALVE
CHARCOAL PUMP
LEVER
GE SAMPLE
POLARIZER
PROBE CAP
FILTER
MYLAR WINDOW
DETECTOR LIGHTPIPE
LIQUID HE3 CAN
DETECTOR
CARBON RESISTOR

gold grid polarizer on a Mylar substrate (Buckbee-Mears Company) polarized the transmitted radiation parallel or perpendicular to the stress axis. The direction of the FIR polarization could be selected from outside the cryostat. The outgoing FIR beam was filtered, then guided by a light pipe through a 0.0005" thick Mylar window to the detector. Also shown in Fig. 2-2 is the calibrated stress device used to apply a force on the sample. The force was produced by the compression of two springs and was transmitted to the sample through a system of levers and rods.

During the experiments done in exchange gas, the sample temperature was controlled by a Cu-Au (7% Fe, annealed) thermocouple in combination with a heater. The sample temperature could be varied from 3 K up to 20 K. At higher temperatures, the sample chamber was kept under vacuum to insulate the sample from the ^{4}He cryostat.

The detector output was directly amplified and recorded by a nova II computer (Data General Corp.) via a A/D converter (Michelson interferometer) or was detected by phase sensitive detection with an Ithaco Dynatrac 3 Lock-in Analyser (Martin-Pupplett interferometer). The first harmonic signal was then transmitted through a voltage to frequency converter and a counter to the computer. The computer controlled the interferometers through several interfaces and collected the detector output as a function of mirror position. The resulting interferograms were apodized,

phase corrected and Fourier transformed giving the relative transmitted intensity as a function of frequencies. The computer averaged the spectra and calculated the absorptance of excitons. The results of the experiments were stored on floppy diskettes and transferred to a LSI - 11/23 computer (Digital Equipment Corp.) for further analysis.

2.5 Stress System and Calibration

Figure 2-3 shows the stress system used to apply a force on the sample. A micrometer located on top of the probe varied the compression of two springs with a total force constant of 13.4 ± 0.2 kg/cm [18]. The force was transmitted from the micrometer to a 3.2 mm diameter steel pull rod attached to a right angle lever with a cylindrical bearing. This lever pressed against a cylindrical brass piston on the sample. The geometry of the lever dictated that the force applied to the piston was 9.0±0.1 times the force at the bearing-lever joint. The purpose of the cylindrical bearing was to prevent any non-vertical force at the lever contact while the ball bearing avoided any non-horizontal force on the piston. The sample was compressed between the piston and a brass wall bolted to the probe. Thin indium pads were inserted at the sample/wall and sample/piston interfaces to avoid non-uniform strain in the sample. The system was prestressed at room temperature to compress the pads and hence obtain good stress reproducibility and good thermal contacts.

Fig. 2-3

Cross-sectional detail of the probe sample holder, showing part of the stress system. The pull-rod was attached to the spring and micrometer screw at the top of the cryostat. It transmitted force to the right-angle lever through a cylindrical bearing. The lever pivoted on a steel rod which passed through the probe block, and transmitted force to the piston through a fixed ball bearing. The variable-position wall was securely bolted during the experiments. (Figure taken from Scholes [16]).

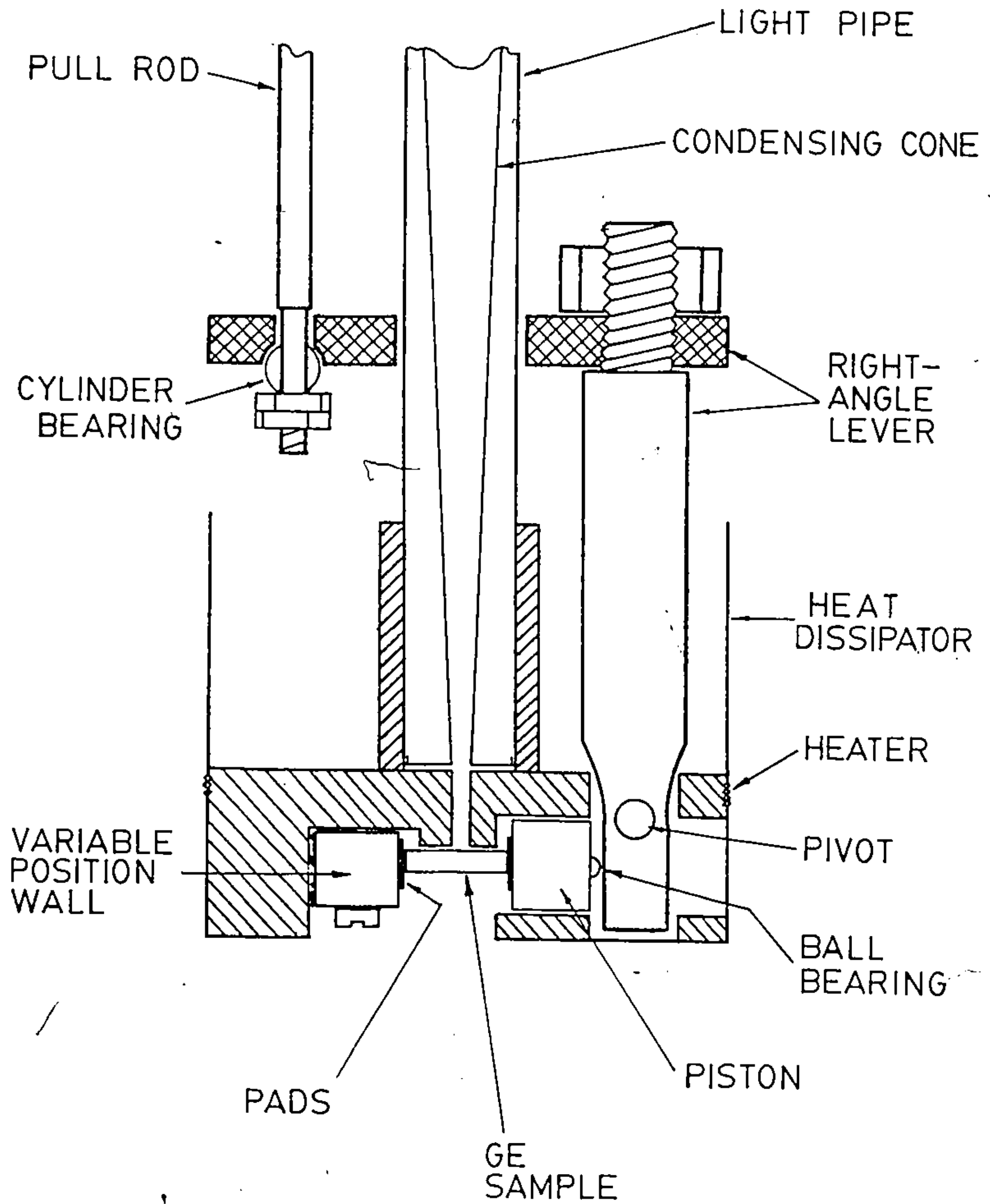
LIGHT PIPE
PULL ROD
CONDENSING CONE
CYLINDER BEARING
RIGHT-ANGLE LEVER
HEAT DISSIPATOR
HEATER
VARIABLE POSITION WALL
PIVOT
BALL BEARING
PISTON
PADS
GE SAMPLE

A calibration of the stress system was carried out because of possible frictional torques, elastic bending and stretching in our system. The sources of friction may be located, for example, at the pull-rod/lever joint, level pivot and lever/piston contact while the bending may be experienced in the brass arm of the lever and possibly some stretching of the pull-rod. These possible losses would tend to reduce the force on the sample below the value given by the product of the spring constant, spring contraction and the level factor (9.0).

A stress sensor was built from a capacitive sensor and a LC Armstrong-type radio-frequency oscillator [19]. A schematic diagram of the oscillator is illustrated in Fig. 2-4. The oscillator was composed of a dual-gate N-channel depletion type MOSFET (RCA #40673), two Silver-Mica (Miconics) capacitors, one Metallized film type (Philips) capacitor, a sensor capacitor C_s, five resistors (Ohmite), and three inductors. The inductors were made with a 40 AWG Single Polyester-Imide coated copper wire (Belden) mounted on a 1 cm diameter by 10 cm long plexiglass rod. The resulting coils L_1, L_2, and L_3 had 760, 787, and 18 turns respectively. The capacitor C_s was connected to the oscillator with a 23" long 30 AWG coaxial cable (Belden #9221). The cable and the capacitor C_s at zero stress had a capacitance of 33 pF and 30 pF respectively. The frequency of oscillations was mainly determined by L_2 and C_s + 33 pF. The circuit components were

Fig. 2-4

Circuit diagram of the oscillator employed with the stress sensor to calibrate the stress system. The oscillator operated at a resonant frequency of 2 MHz which was monitored by observing the induced voltage appearing across the pick-up coil L_3. The number of turns of the coil was chosen sufficiently small to minimize any disturbance by the co-axial cable on the oscillator frequency. The values used for the different components in the circuit are:

$R_1 = 150\ k\Omega$

$R_2 = 1.5\ k\Omega$

$R_3 = 6.8\ k\Omega$

$R_4 = R_5 = 100\ \Omega$

$C_1 = 2.5\ nF$

$C_2 = 2.2\ nF$

$C_3 = 68\ nF$

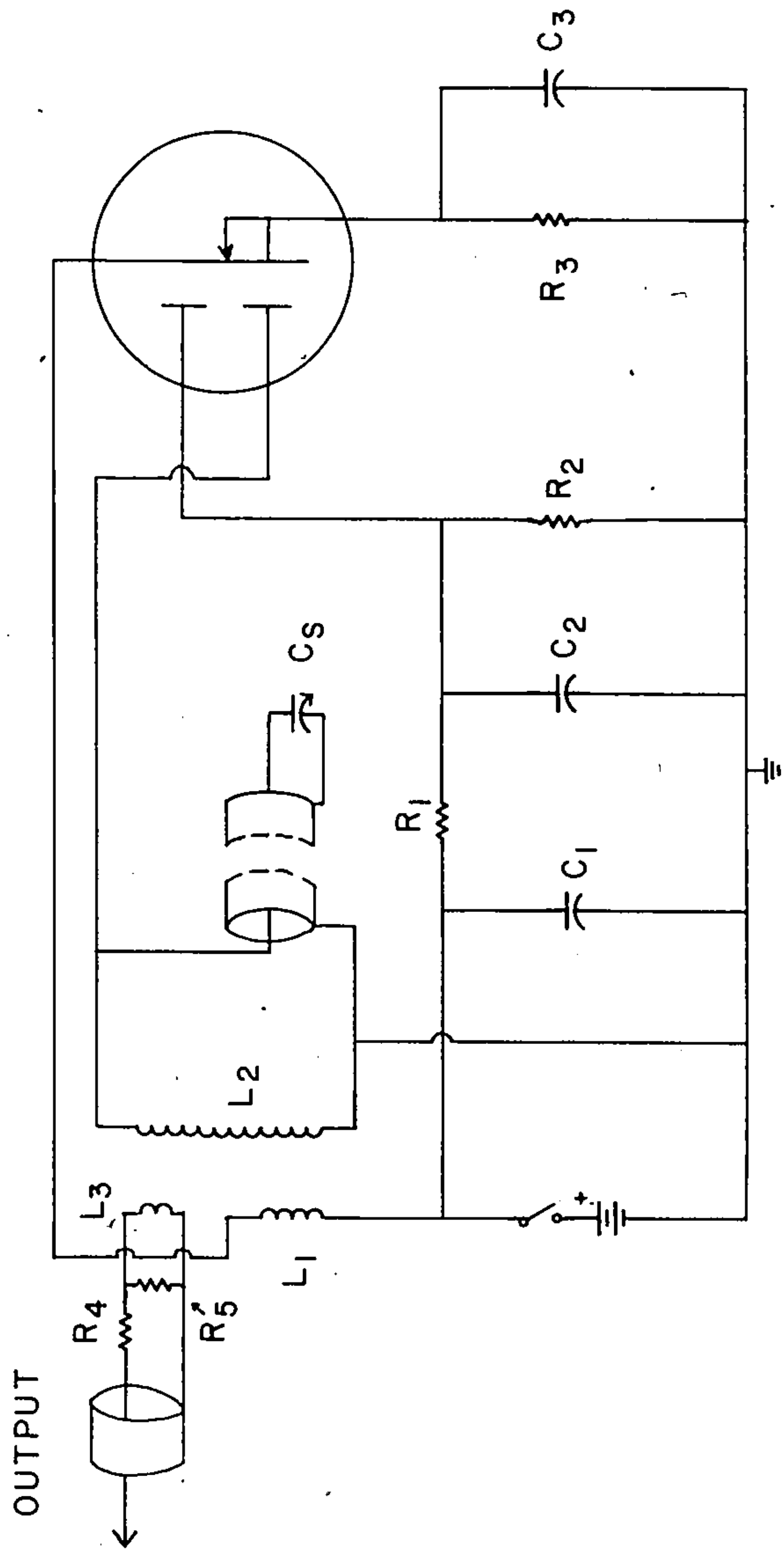

C3
R3
R2
C2
Cs
R1
C1
L2
L3
L1
R4
R5
OUTPUT

optimized to produce an undistorted sine wave at a frequency of 2 MHz and a peak to peak output voltage of 0.3 volts at a bias voltage of 12 volts. The circuit operated above 55 K. Below this temperature the carriers in the MOSFET froze out. A schematic diagram of the capacitive stress sensor is shown in Fig. 2-5. All sensor components were machined from a rod of Beryllium Copper Brush #25 Alloy which was initially heat treated at a temperature of 600°F for three hours and then air cooled to ambient temperature. The resulting Rockwell hardness C-42 indicated that the alloy had the high yield strength required for the sensor. The right hand capacitor plate was electrically insulated from the body of the sensor with two 0.007" thick cover glass spacers and epoxy (Miller-Stephenson Chemical Co., Inc. #907). The body of the sensor and the left hand capacitor plate were tightly bolted together with two Beryllium Copper screws. The separation between the plates was 25 μm at zero stress. The two leads of the coaxial cable were respectively connected to the left hand plate with a screw and to the right hand plate with silver paste. The stress sensor was calibrated by applying known forces on the right hand capacitor plate through a brass dummy sample which had the same dimensions as the Ge crystal. The calibration was done at 77 K in a two step process. First the oscillator frequency was measured as a function of the

Fig. 2-5

Cut-away schematic drawing of stress system with stress sensor. View is from bottom of cryostat. The body of the stress sensor was machined from two Be-Cu parts and bolted tightly together. The right hand capacitor plate was glued to the body of the sensor through insulating glass slabs. The plate separation was 25 μm (not to scale) at zero stress. Crystallographic directions are indicated by the triad. For experimental runs the sensor was replaced by a solid brass wall. (Figure taken from Scholes [16]).

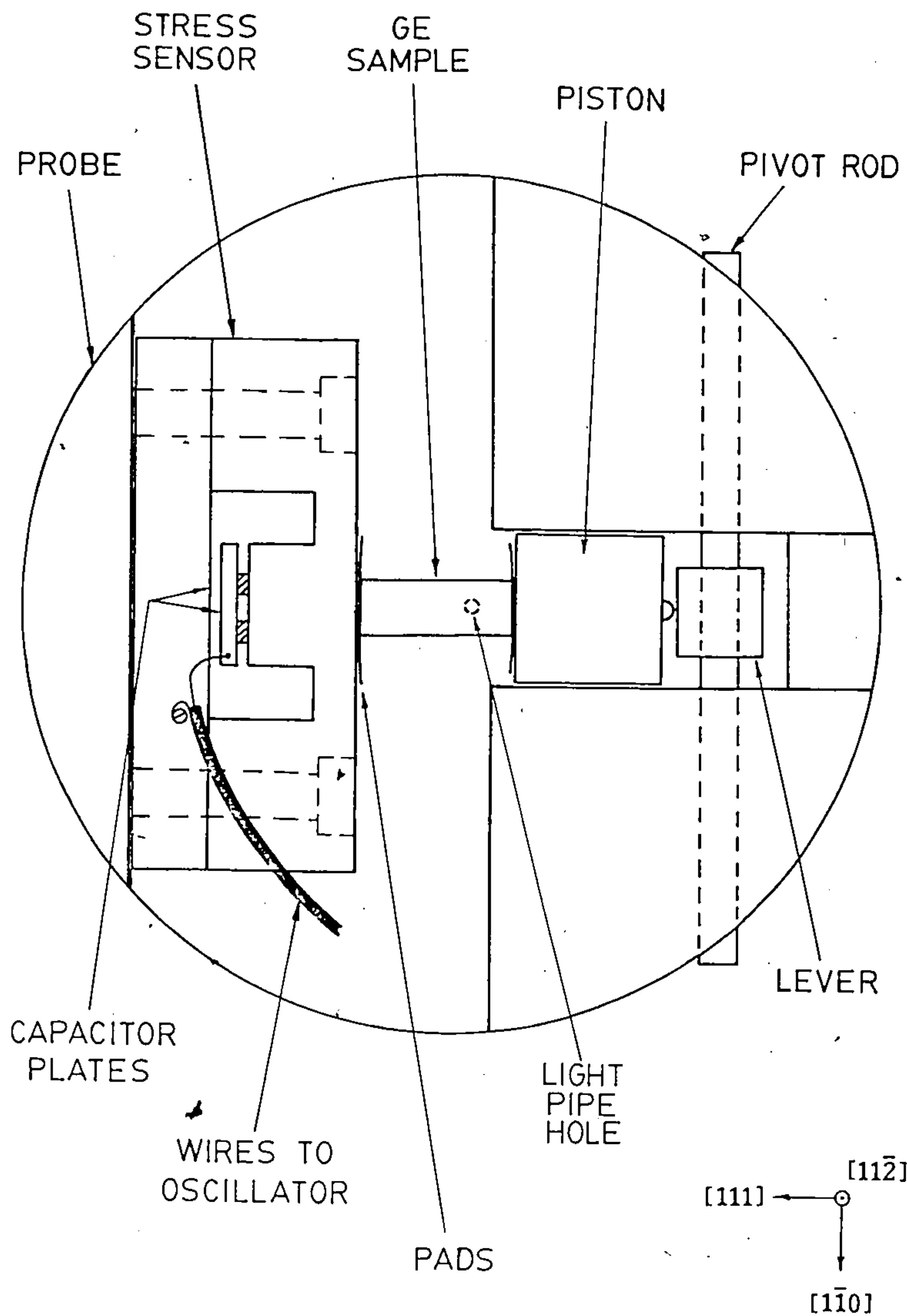

STRESS SENSOR
GE SAMPLE
PISTON
PROBE
PIVOT ROD
CAPACITOR PLATES
WIRES TO OSCILLATOR
PADS
LIGHT PIPE HOLE
LEVER
[111]
[11$\bar{2}$]
[1$\bar{1}$0]

known force. Then by recording the oscillator frequency as a function of spring length the forces on the Ge sample were obtained. To use the sensor at 1.2 K required an indirect approach. Since at this temperature it was not possible to apply any known forces on the sensor the 77 K sensor calibration was extrapolated to 1.2 K by using the temperature dependence of the Young modulus of elasticity of Beryllium Copper [20] and the static dielectric constant of He^4 liquid [21]. Finally, from the measurements of the oscillator frequency as a function of spring length the forces on the sample were derived at 1.2 K.

The results of this analysis showed that the calibration carried out with the stress sensor agreed to within ∿ 10% with the mechanical calibration obtained from the product of the spring length, spring constant, and the geometric lever factor (9.0±0.1). At maximum spring contraction, the two springs had an S shape, rendering a direct measurement of the spring length very uncertain. In this case, the sensor calibration was used to obtain the force on the sample. The stress system did suffer from small elastic bending of the brass arm of the lever and possibly some stretching of the steel pull-rod. To further check the mechanical calibration, Scholes [16] compared his EHD luminescence data as a function of stress with those obtained by other groups who were able to use more ideal stress systems. From the good agreement between his data

and others, he concluded that the mechanical calibration was correct within $\sim$ 10%.

CHAPTER 3

FAR-INFRARED ABSORPTION SPECTRUM OF EXCITONS IN [111]-STRESSED GERMANIUM: HIGH STRESS LIMIT

3.1 Introduction

The most detailed information on the internal structure of free excitons in germanium was obtained by the far-infrared (FIR) absorption experiments [22-27,17]. In these experiments, transitions from the even parity ground states to the odd parity excited states were observed. Furthermore, the energy of the even parity ground states was measured by examining the FIR exciton photoconductivity [28] and by looking at the derivative of the near infrared absorption edge [29]. To interpret this series of experimental results, a comprehensive theoretical treatment of the exciton energy spectrum was made [30-32]. Despite the complicated band structure, good agreement between calculated and measured energy levels was obtained. Nevertheless, some of the observed transitions were not predicted and some of the predicted transitions have not been observed.

Application of a uniaxial compressive stress along the [111] direction simplifies the band structure. In the presence of very large stresses, excitons are formed from one conduction band and one valence band. Both bands are ellipsoids of revolution with their major axis along the

[111] direction. The resulting energy spectrum of excitons is very simple. Muro and Narita [33], and Yamanaka et al. [34] determined, from their FIR magnetoabsorption of excitons at intermediate stresses, an exciton ground state energy of ≈ 2.75 meV. Feldman et al. [35] measured from the luminescence of excitons at intermediate stresses a binding energy of (2.3±.4) meV and (2.6±1.2) meV, respectively. These experiments were not able to provide any detail on the exciton spectrum at very large stresses, where the simplification of the band structure would be most noticeable.

The purpose of this study was to determine the energy spectrum of excitons at very large stresses. The FIR absorption spectra were measured as a function of stress from 9 to 38 kg/mm^2 [18], and as a function of the direction of the FIR polarization with respect to the stress axis. At high stress, the exciton spectra are similar to those of donors [36]. A theoretical model is used to predict the energy levels and the relative absorption of transition lines. Good agreement is observed between theory and experiment.

In the next section, a description of the Ge band structure as a function of stress is presented. The exciton Hamiltonian derived from the band structure at very large stress is solved by using a variational method. The method of calculation and the numerical results are given in section 3.3. Finally, the experimental results are presented with

a comparison of the model in section 3.4.

3.2 Band Structure of Germanium

Germanium has the diamond structure which consists of a FCC Bravais lattice with a two-atom basis (0,0,0) and a $(\frac{1}{4},\frac{1}{4},\frac{1}{4})$, where a is the lattice constant. The relevant bands of Ge for this work are shown in Fig. 3-1 [37]. Ge has an indirect band gap of 0.744 eV at 0 K. A consequence of the indirect gap is that optical recombination must be assisted with the emission or absorption of a phonon in order to conserve crystal momentum. This makes optical recombination a slow process and hence the origin for the long lifetime of excitonic systems in Ge. The maximum of the valence band occurs at the centre of the Brillouin zone. In absence of spin-orbit coupling, the valence band at $\underset{\sim}{k} = 0$ is sixfold degenerate. It is formed from the p-states of the free atom. The spin-orbit interaction partially lifts the degeneracy into a fourfold $J = 3/2$ band edge and twofold $J = 1/2$ "split-off" band. The two bands are separated by 0.29 eV at the zone centre. As k increases from zero, the band edge splits into a doubly degenerate heavy hole $M_J = \pm 1/2$ and light hole $M_J = \pm 3/2$ bands. The wavevector dependence of the band edge near $k = 0$ is [38]:

$$E_{\substack{H \\ L}}(\underset{\sim}{k}) = Ak^2 \mp [B^2k^4 + C^2(k_x^2k_y^2 + k_y^2k_z^2 + k_z^2k_x^2)]^{1/2} , \qquad (3-1)$$

where H and L stand for heavy and light hole band respect-

Fig. 3-1

Calculated energy band structure of Ge for two directions of wavevector k. Only the bands closest to the bandgap are shown. The labels correspond to conduction (C), heavy hole (Hh), light hole (Lh), and split-off hole (Soh) bands. The indirect bandgap is 744 meV (0°K) between the conduction band L-point and the valence band Γ-point. The Lh and Hh bands are degenerate at the Γ-point, while the Soh band is at -290 meV. (Figure taken from Scholes [16].

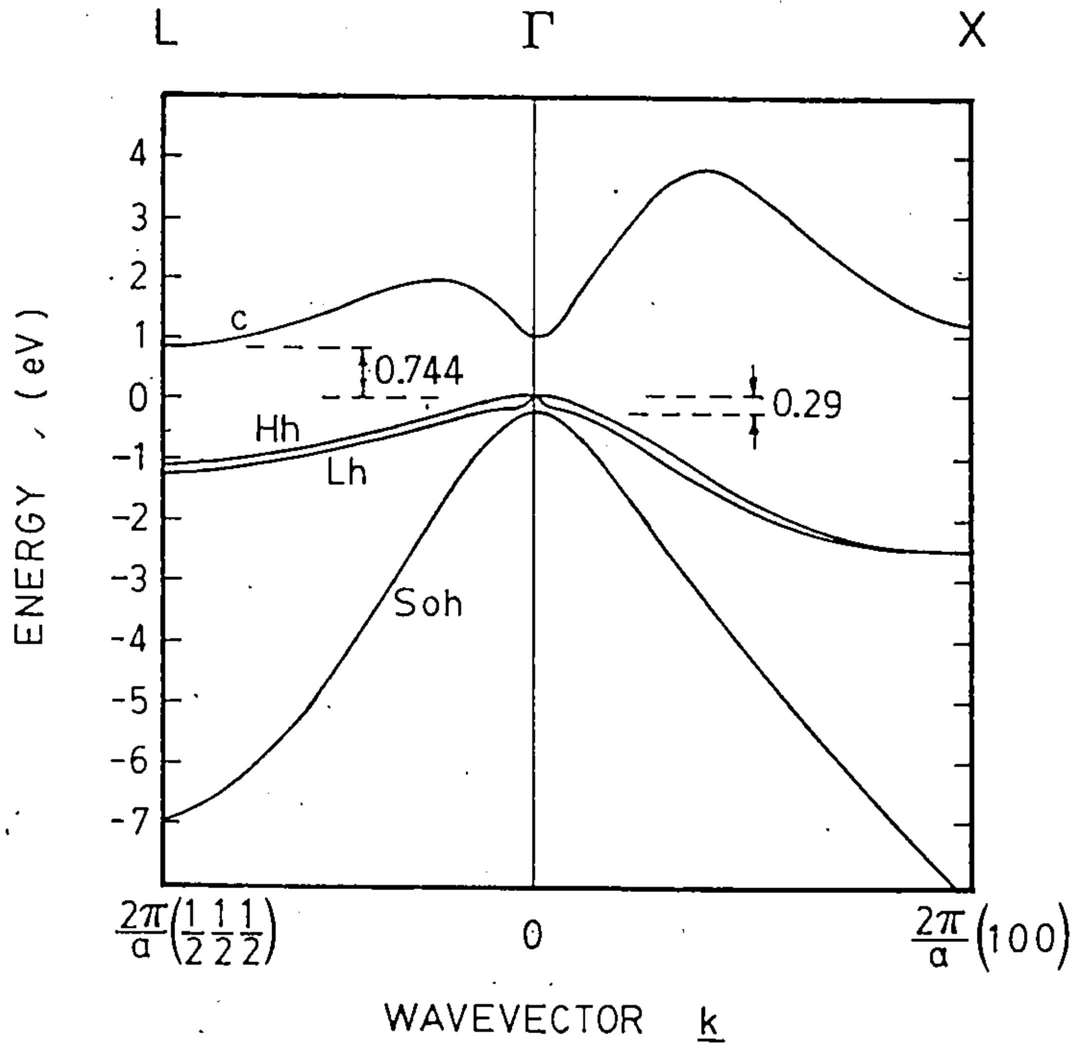
L
Γ
X
4
3
2
1
0
-1
-2
-3
-4
-5
-6
-7
c
0.744
0.29
Hh
Lh
Soh
ENERGY , (eV)
$\frac{2\pi}{a}\left(\frac{1}{2}\frac{1}{2}\frac{1}{2}\right)$
0
$\frac{2\pi}{a}(100)$
WAVEVECTOR k

ively. The parameters A, B and C are listed in Table 3-1.

The conduction band edge is located at the zone boundary $\frac{\pi}{a}$ (1,1,1). As a consequence of the crystal symmetry, there are four equivalent energy minima. The constant energy surface near these minima is an ellipsoid of revolution with the major axis along the <111> direction and is characterized by transverse and longitudinal effective masses, m_{et} and m_{el} respectively. Levinger's and Frankl's [39] values of m_{et} and m_{el} are given in Table 3-1.

Application of uniaxial compressive stress S along the [111] direction reduces the cubic symmetry of the crystal and therefore removes some of the band degeneracies. Figure 3-2 shows the deformation of the band structure as a function of stress. The conduction band ellipsoid whose major axis is along the [111] direction is lowered in energy with respect to the other three. The separation between the upper and lower valleys is $\Delta_e = 1.03|S|$ meV mm^2/kg [40]. The valence band edge splits into two doubly degenerate states $M_J = \pm 1/2$ and $M_J = \pm 3/2$. As the stress increases, the heavy-hole band $M_J = \pm 1/2$ goes up in energy toward the [111] conduction band minimum. The stress dependence of the splitting between the heavy and light hole bands is $\Delta_h = 0.363|S|$ meV mm^2/kg [41a]. Despite their splitting at $\underset{\sim}{k} = 0$, significant coupling between the bands remains until large stresses. In the limit of high stresses, the hole

Table 3-1

Band structure parameters for Ge

$A = 13.38$ [a]

$B = 8.48$ [a]

$C = 13.14$ [a]

$m_{et} = 0.08152$ [b]

$m_{el} = 1.588$ [b]

$m_{ht} = 0.13000$ [c]

$m_{hl} = 0.0403$ [c]

$m_{oe} = 0.1192$ [d]

$m_{oH} = 0.2754$ [e]

$m_{oL} = 0.04210$ [e]

$\varepsilon_o = 15.36$ [f]

[a] The parameters, A, B and C were obtained from γ_1, γ_2 and γ_3 of Hensel and Suzuki [41a] with the transformations given by Kelso [41b].

[b] See ref. 39.

[c] See ref. 41a.

[d] $m_{oe}^{-1} = (m_{el}^{-1} + 2m_{et}^{-1})/3$.

[e] See ref. 41b.

[f] See ref. 42.

Fig. 3-2

Band structures of Ge as a function of stress. The band structure at zero and finite stress are shown on the left and right hand side respectively. At zero stress, the band structure is composed of four equivalent conduction band minima along the <111> directions and fourfold degenerate valence band. Upon application of stress along the [111] direction, the [111] conduction band minimum lowers in energy with respect to the other three. Their separation is Δ_e. The valence band edge splits into two bands. The heavy hole band moves up in energy and is separated by Δ_h from the light hole band.

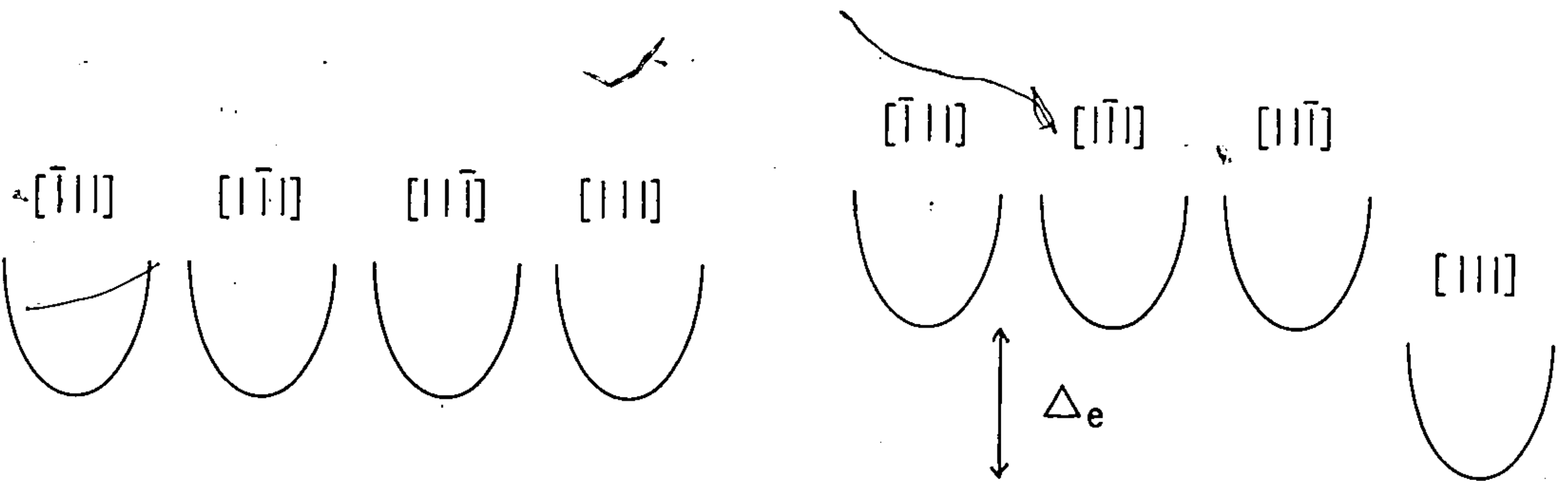

[111] STRESS

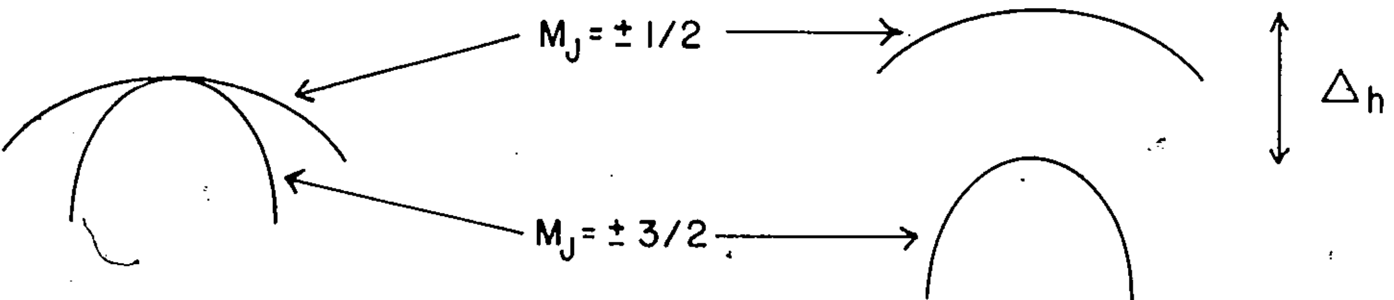

bands become ellipsoids of revolution with their major axis along the [111] direction. In this limit, the effective masses of the valence bands were measured by Hensel and Suzuki [41a]. Their values are given in Table 3-1. They also observed that the effective masses of the conduction band do not vary with stress. Therefore, the effective masses of the conduction band measured by Levinger and Frankl [39] will be used in the following calculation.

3.3 Theoretical Model for the Energy Levels of Excitons in [111]-Stressed Germanium

In the effective mass approximation the exciton Hamiltonian is

$$H_{ex} = H_e(\underset{\sim}{p}_e) + H_h(\underset{\sim}{p}_h) - \frac{e^2}{\varepsilon_0 |\underset{\sim}{r}_e - \underset{\sim}{r}_h|} ; \qquad (3\text{-}2)$$

where the subscripts e and h refer to the electron and hole respectively, $\underset{\sim}{p}$ is the momentum conjugate to $\underset{\sim}{r}$ and ε_0 is the static dielectric constant. At very large stress $H(\underset{\sim}{p})$ in the above equation takes the form

$$H(\underset{\sim}{p}) = \frac{1}{2m_t}(p_1^2 + p_2^2) + \frac{1}{2m_\ell} p_3^2 , \qquad (3\text{-}3)$$

where m_ℓ and m_t are the longitudinal and transverse masses respectively, and p_3 is the momentum component along the [111] direction. To solve the Schrödinger equation associated with Hamiltonian (3-2) we make the following transformation of coordinates (Altarelli and Lipari [31])

$$\underset{\sim}{r} = \underset{\sim}{r}_e - \underset{\sim}{r}_h \ ,$$
$$\underset{\sim}{R} = \alpha \underset{\sim}{r}_e + \beta \underset{\sim}{r}_h \ , \tag{3-4}$$

where α and β are 3×3 matrices and α and β satisfy $|\det(\alpha+\beta)| = 1$. The conjugate momenta are given by

$$\underset{\sim}{p}_e = \alpha \underset{\sim}{P} + \underset{\sim}{p} \ ,$$
$$\underset{\sim}{p}_h = \beta \underset{\sim}{P} - \underset{\sim}{p} \ . \tag{3-5}$$

By analogy to the hydrogen problem, we choose

$$\alpha = \begin{pmatrix} m_{et}/M_t & 0 & 0 \\ 0 & m_{et}/M_t & 0 \\ 0 & 0 & m_{e\ell}/M_\ell \end{pmatrix} , \ \beta = \begin{pmatrix} m_{ht}/M_t & 0 & 0 \\ 0 & m_{ht}/M_t & 0 \\ 0 & 0 & m_{h\ell}/M_\ell \end{pmatrix} \tag{3-6}$$

where $M_t = m_{et} + m_{ht}$, $M_\ell = m_{e\ell} + m_{h\ell}$, and $|\det(\alpha+\beta)| = 1$ is satisfied. The exciton Hamiltonian becomes

$$H_{ex} = \left(\frac{P_1^{\ 2}+P_2^{\ 2}}{2M_t} + \frac{P_3^{\ 2}}{2M_\ell} \right) + \left(\frac{p_1^{\ 2}+p_2^{\ 2}}{2\mu_t} + \frac{p_3^{\ 2}}{2\mu_\ell} - \frac{e^2}{\varepsilon_0 r} \right)$$
$$= H_{cm} + H_r \ , \tag{3-7}$$

where $\mu_\ell^{-1} = m_{e\ell}^{-1} + m_{h\ell}^{-1}$ and $\mu_t^{-1} = m_{et}^{-1} + m_{ht}^{-1}$. We now introduce the effective Rydberg and the effective Bohr radius,

$$R_0 = \frac{\mu_t e^4}{2\hbar^2 \varepsilon_0^{\ 2}} \ , \qquad a_0 = \frac{\hbar^2 \varepsilon_0}{\mu_t e^2} \ , \tag{3-8}$$

as units of energy and length, respectively. H_r expressed

in reduced units becomes

$$H_r = -\left(\frac{\partial^2}{\partial x^2} + \frac{\partial^2}{\partial y^2} + \gamma\,\frac{\partial^2}{\partial z^2}\right) - \frac{2}{\sqrt{x^2+y^2+z^2}}\ , \tag{3-9}$$

where $\gamma = \mu_t/\mu_\ell$. By using the electron and hole effective masses of Levinger and Frankl [39], and Hensel and Suzuki [41a], respectively, and the static dielectric constant of Faulkner [42]

$$\begin{aligned} \gamma &= 1.275\ , \\ R_0 &= 2.889\ \text{meV}\ , \\ a_0 &= 162.2\ \text{Å}\ . \end{aligned} \tag{3-10}$$

The Hamiltonian H_r given in Eq. (3-9) for the relative motion of exciton in the high stress limit is formally identical to the donor Hamiltonian. The donor problem was first analysed by Kohn and Luttinger [43]. They observed that H_r is invariant under a rotation around the z axis and under inversion, hence, the z component of the angular momentum, m, and the parity, P, are conserved. However, all states with the same m and P are mixed. They calculated with a variational method the 1S, $2P_0$, $2P_\pm$, 2S and $3P_0$ energy levels by using a single trial function for each eigenfunction. The subscripts 0 and ± stand for $m = 0$ and $m = \pm 1$. Faulkner [42] solved the problem by expanding each eigenfunction into a linear combination of trial functions. However, these authors treated the problem for $\gamma \leq 1$ where-

as for the exciton problem, $\gamma = 1.275$. Keyes [44] repeated the calculation of Kohn and Luttinger only for the 1S level with $\gamma \geq 1$ and with an anisotropic, static dielectric constant. We reproduced Kohn and Luttinger's variational calculation for the 1S, $2P_0$ and $2P_\pm$ levels and $\gamma \geq 1$. Their normalized wavefunctions are given in Table 3-2. These single variational wavefunctions represent the low lying levels very well [42]. Nevertheless, this method only yields upper bounds of the energy levels. The method of calculations together with the analytical results are presented in appendix A.

The calculated 1S, $2P_0$ and $2P_\pm$ energy levels as a function of γ are shown in Fig. 3-3. From Fig. 3-3, it is seen that the $2P_0$ energy level lies higher in energy than the $2P_\pm$ level. Therefore, the line centre of the 1S-$2P_0$ transition, ν_0 will be on the high energy side of the line centre of the 1S-$2P_\pm$ transition, $\nu_\pm$. The line positions are inverted with respect to the donor ones. This line inversion is easily understood since for $\gamma > 1$, $\mu_t > \mu_\ell$ hence, the transverse component of the kinetic energy is smaller than the longitudinal one. The resulting binding energy of the $2P_\pm$ state will be bigger than the $2P_0$ state.

To have an estimate of the strength of the 1S-2P transitions, one can evaluate the relative absorption associated with those transitions. In the presence of an electromagnetic wave the electron and hole momenta become

Table 3-2

Variational wavefunctions for the low-lying levels of excitons.

$$\psi_{1S}(\underset{\sim}{r}) = \frac{1}{(\pi a^2 b)^{1/2}} \exp-\left(\frac{\rho^2}{a^2} + \frac{z^2}{b^2}\right)^{1/2}$$

$$\psi^0_{2P}(\underset{\sim}{r}) = \frac{1}{(\pi a^2 b^3)^{1/2}} \, z \exp-\left(\frac{\rho^2}{a^2} + \frac{z^2}{b^2}\right)^{1/2}$$

$$\psi^{\pm}_{2P}(\underset{\sim}{r}) = \frac{1}{(\pi a^4 b)^{1/2}} \, x \exp-\left(\frac{\rho^2}{a^2} + \frac{z^2}{b^2}\right)^{1/2}$$

where $\rho^2 = x^2 + y^2$ and, a and b are the variational parameters.

Fig. 3-3

Calculated 1S, $2P_0$ and $2P_\pm$ energy levels as a function of the reduced mass ratio, $\gamma = \mu_t/\mu_\ell$, of exciton in the high stress limit. The vertical arrow indicates the value of γ for excitons in Ge. Notice, the hydrogen energy levels are given by $\gamma = 1$.

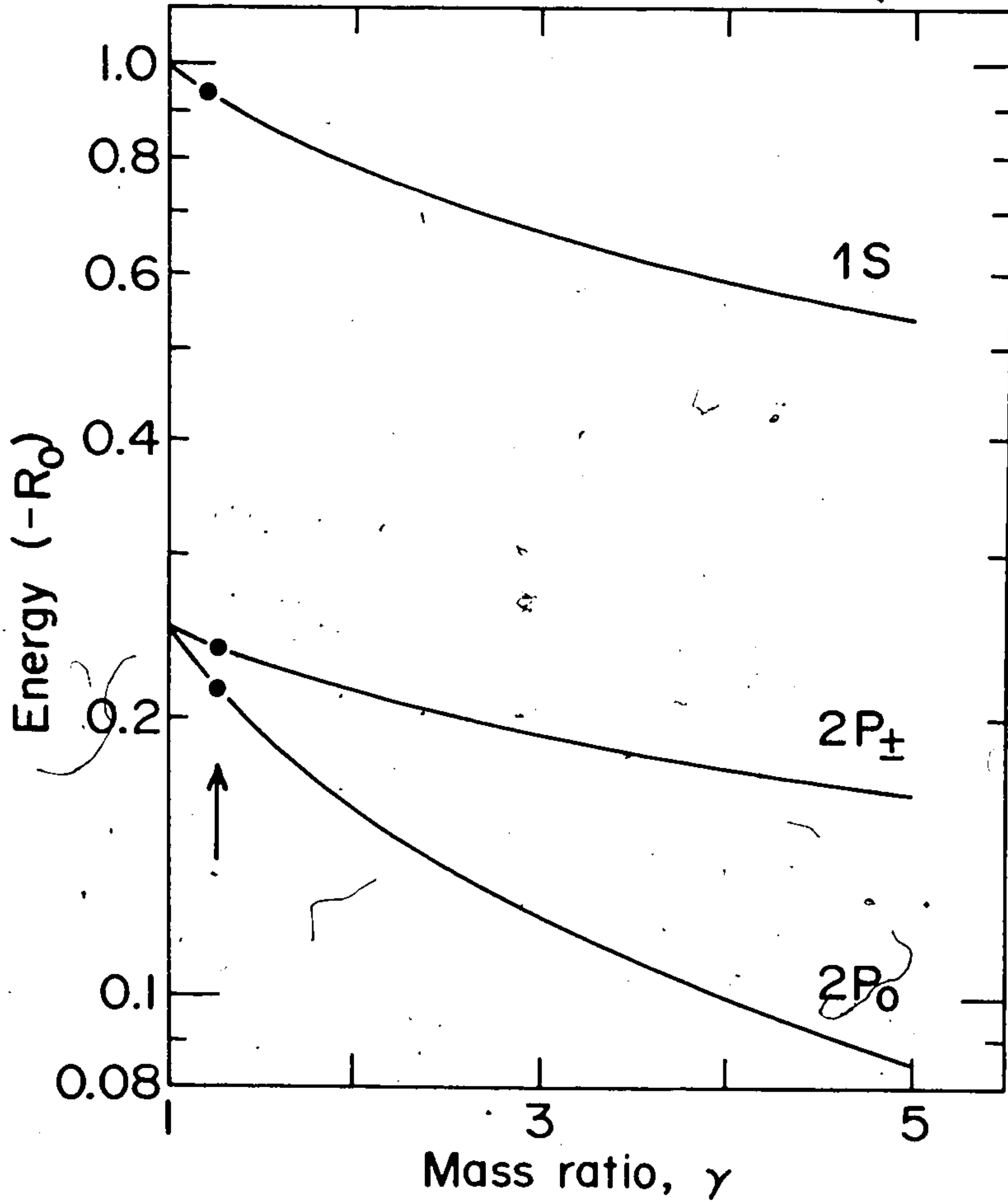

Energy (-R_o)
1.0
0.8
0.6
0.4
0.2
0.1
0.08
1S
2P±
2P₀
1
3
5
Mass ratio, γ

$$\underset{\sim}{p}_e + \frac{e}{c} \underset{\sim}{A}(\underset{\sim}{r}_e, t) ,$$
$$\underset{\sim}{p}_h - \frac{e}{c} \underset{\sim}{A}(\underset{\sim}{r}_h, t) . \quad (3\text{-}11)$$

In the following, we will use the dipolar approximation and the Coulomb gauge. By using the above momenta the transformation (3-5) applied to the original Hamiltonian (3-2) gives the same final H_{ex} in Eq. (3-7) except p_n is replaced by $p_n + \frac{e}{c} A_n$. After a few algebraic manipulations, the absorption coefficient, α, of excitons is proportional to [46]

$$\alpha \propto \nu_{if} |\sum_n \varepsilon_n \langle i|x_n|f\rangle|^2 , \quad (3\text{-}12)$$

where $\underset{\sim}{\varepsilon}$ is a unit polarization vector, ν_{if} is the transition frequency between the initial, $|i\rangle$, and the final, $|f\rangle$ state. Hence, for polarization, $\underset{\sim}{E}$, parallel to the stress axis, $\underset{\sim}{E} \parallel \underset{\sim}{S}$, the only optical transition observed is from the 1S to $2P_0$ state. For polarization $\underset{\sim}{E}$ perpendicular to the stress axis, $\underset{\sim}{E} \perp \underset{\sim}{S}$ the only optical transition observed is from the 1S to $2P_{\pm}$ state. The relative absorption of the $1S - 2P_0$ transition to the $1S - 2P_{\pm}$ transition is

$$\frac{\alpha_0}{\alpha_{\pm}} = \left(\frac{\nu_0}{\nu_{\pm}}\right) \times \left(\frac{\langle 1S|z|2P_0\rangle}{\langle 1S|x|2P_{\pm}\rangle}\right)^2 . \quad (3\text{-}13)$$

An estimate of the matrix elements is obtained by using the variational wavefunctions. The relative absorption becomes

$$\frac{\alpha_0}{\alpha_{\pm}} \approx 1.4 . \quad (3\text{-}14)$$

The numerical value is expected to be accurate within a factor three to four because of the variational method used. A comparison between the theoretical and experimental results will be given in the next section.

3.4 Experimental Results and Discussion

Measured absorption spectra of excitons are shown in Fig. 3-4. These spectra were taken at $T = 1.2$ K, and for each stress value, a spectrum was taken with $\underset{\sim}{E} \parallel \underset{\sim}{S}$ and $\underset{\sim}{E} \perp \underset{\sim}{S}$. The laser power was the same for all spectra, hence the evolution in relative absorption can be observed. The upper part of Fig. 3-4 shows an absorption spectrum taken at $S = 19$ kg/mm^2 and $\underset{\sim}{E} \parallel \underset{\sim}{S}$. At this stress value the separation between the lower and upper conduction bands is 19.6 meV. Excitons formed with electrons in the upper conduction bands exist at lower stresses but at these high stresses intervalley scattering depopulates the upper bands [47]. A strong line associated with the $1S\text{-}2P_0$ transition at 2.32 meV is observed among several weak lines. Also observed in the spectrum is a shoulder located on the low energy side of the $1S\text{-}2P_0$ transition. The shoulder and the weak lines may be related to residual warping of the valence bands. The background observed at $\sim$ 3 meV in the spectrum is caused by the absorption of electron-hole drops (EHD) [48]. The same features are also observed in the spectrum with $\underset{\sim}{E} \perp \underset{\sim}{S}$. A strong absorption line observed at

Fig. 3-4

Far-infrared absorption spectra of excitons in Ge as a function of uniaxial [111] stress. For each stress value a spectrum was taken with the FIR polarization parallel and perpendicular to the stress axis. The laser power was the same for all spectra. The labels in the spectra indicate the 1S-2P and 1S-3P transitions. Notice the shift in energy of the absorption lines as the stress increases. The shift is produced by a continuous decoupling of the valence bands.

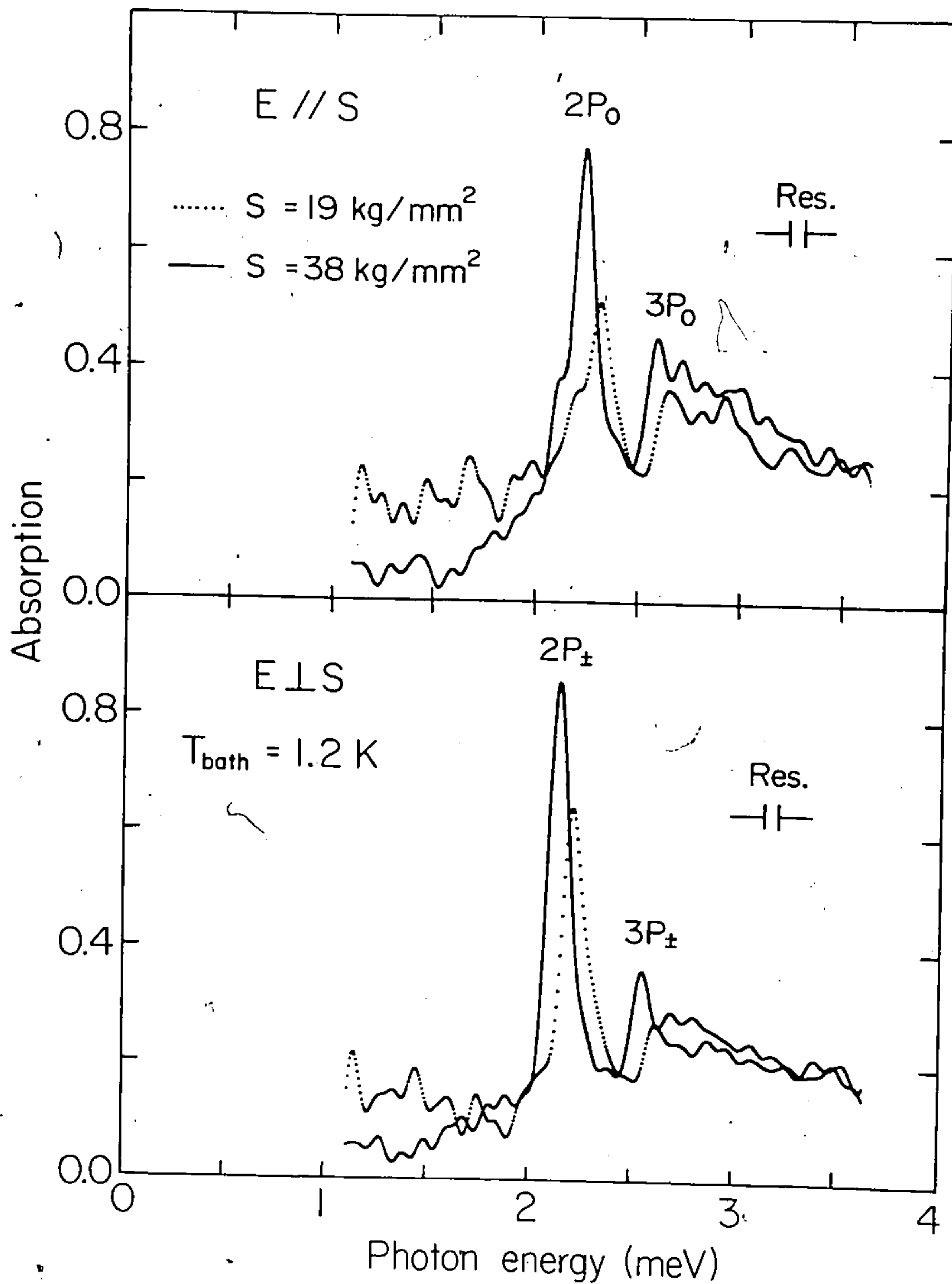

E // S
2P0
S = 19 kg/mm2
S = 38 kg/mm2
Res.
3P0
0.8
0.4
0.0
Absorption
E⊥S
Tbath = 1.2 K
2P±
3P±
Res.
0.8
0.4
0.0
0
1
2
3
4
Photon energy (meV)

2.22 meV is identified with the 1S-$2P_{\pm}$ transition. As the stress increases from 19 to 38 kg/mm^2, the 1S-2P transitions shift toward lower energy due to a continuous decoupling of the valence bands. This decoupling is also reflected on the high energy side of the 1S-2P transitions where the spectrum of the weak lines varies with stress. The absorption spectrum of excitons at stress S $\geq$ 19 kg/mm^2 shows another transition located at $\sim$ 2.6 meV which becomes sharper with stress. We interpret this absorption line as the 1S-3P transition. This transition also has a dependence on polarization. At S = 38 kg/mm^2, the ratio of absorption in both polarizations of the 1S-2P transitions is 0.8±.1. The last ratio compares well with the theoretical estimate of $\alpha_0/\alpha_{\pm} \approx 1.4$.

In order to estimate the line positions at infinite stress, the 1S-2P and 1S-3P line positions as a function of reciprocal stress, 1/S, are plotted in Fig. 3-5. Also shown are the theoretical line positions [49] for 1/S = 0 mm^2/kg. The theoretical values are given in Table 3-3. Notice the increase in curvature of the data points as 1/S goes to zero. The change of curvature suggests that the experimental line positions tend toward the theoretical ones as the stress increases. Furthermore, the observed splittings between the two sets of transitions $2P_0$-$2P_{\pm}$ and $3P_0$-$3P_{\pm}$ converge at high stress to the theoretical values. An extrapolation of

<u>Fig. 3-5</u>

Plot of the exciton line positions as a function of the reciprocal stress $\frac{1}{S}$. The horizontal arrows indicate the theoretical line positions at infinite stress. As the stress increases, the 1S-2P and 1S-3P transitions approach the theoretical line positions corresponding to the high stress limit.

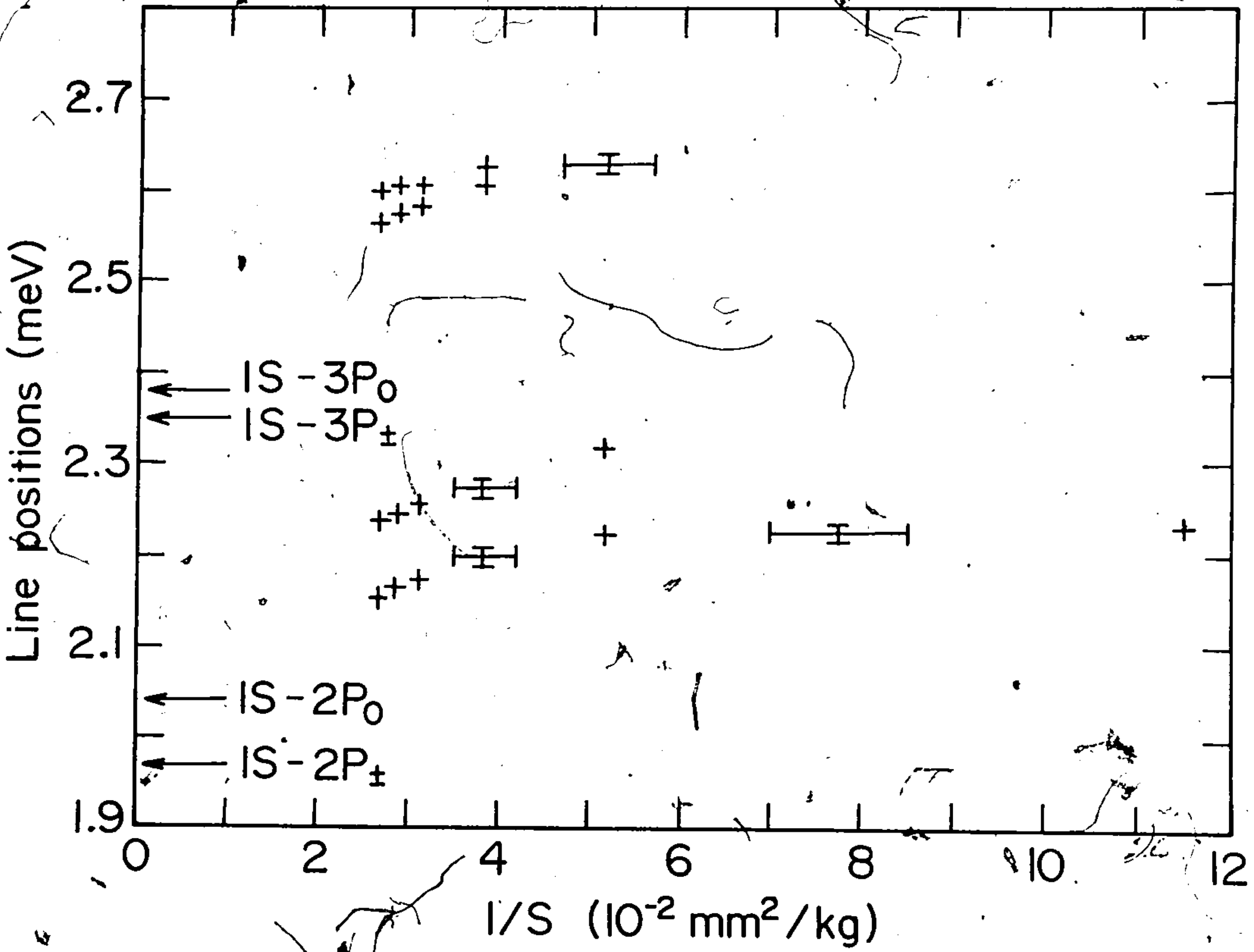

Line positions (meV)
2.7
2.5
2.3
2.1
1.9
1S - 3P$_0$
1S - 3P$_\pm$
1S - 2P$_0$
1S - 2P$_\pm$
0
2
4
6
8
10
12
1/S (10^{-2} mm^2/kg)

Table 3-3

Experimental and theoretical line positions of excitons in the high stress limit.

Transition	Theory ν (meV)	Experiment ν (meV)
$1S-2P_0$	2.04	2.09±.09[a]
$1S-2P_\pm$	1.97	2.02±.08[a]
$1S-3P_0$	2.38[b]	2.5 ±.2[a]
$1S-3P_\pm$	2.35[b]	2.45±.2[a]

[a]The line positions were obtained from a linear extrapolation to $1/S = 0\ mm^2/kg$ using the three data points near $1/S = 0\ mm^2/kg$.

[b]See Ref. 49.

the data points to infinite stress was done. A comparison between the theoretical and extrapolated line positions is shown in Table 3-3. Good agreement is obtained between theory and experiment. This agreement enables us to estimate the binding energy of excitons at infinite stress as 2.70±.08 meV.

In conclusion, although the structure of the exciton energy levels in germanium is not understood very well, it has been shown that in the high stress limit the structure becomes nearly hydrogen like and hence very simple to interpret.

CHAPTER 4

FAR-INFRARED ABSORPTION SPECTRUM OF Be-RELATED BOUND EXCITONS IN SILICON

4.1 Introduction

Prior to this work, the study of bound excitons (BE) was mainly limited to the observation of their even parity states using near-infrared (NIR) spectroscopy. These states are difficult to interpret since they depend on the central cell potential of the binding centre and the line spacing is unique to each impurity. Furthermore, for centres of low symmetry, additional lines due to odd parity excited states can also be observed in the even parity state spectrum making the analysis even more difficult.

In this study, the first far-infrared absorption spectrum of a bound exciton is presented. This spectrum provides information on transitions from the even parity ground states to the odd parity excited states. These odd parity excited states are not shifted by the central cell potential of the binding centre and hence they should give the same spectra. The results of this research show that FIR spectroscopy applied to the study of BE is the best tool for the identification of the BE internal structure.

The Be-related isoelectronic bound exciton (IBE) in silicon was chosen for this study since the IBE lifetime is

very long (∿ 500 μsec) and its concentration is known to be very large (∿ 10^{16} cm^{-3}). These two factors simplify the task of maintaining an observable population of IBE. Furthermore, this centre was carefully studied by using NIR spectroscopy [9,50-51] both in emission and absorption. This makes a direct comparison between FIR and NIR results possible and permits the identification of the BE even parity excited states with known boron impurity excited states. The good agreement between the IBE internal structure and impurity spectra reveals without ambiguity the character of the IBE and corrects the previous understanding of the BE binding centre.

In the next section, Hopfield's model of an IBE will be described. Section 4.3 presents the results on the IBE odd parity excited states together with a comparison between the IBE excited-state spectrum and Hopfield's model.

4.2 Hopfield, Thomas and Lynch Model of an Isoelectronic Bound Exciton

Hopfield, Thomas and Lynch (HTL) [52] developed a model to explain extrinsic absorption and luminescence lines in ZnTe and GaP crystals. They interpreted these transitions as produced by the formation and the recombination of excitons bound at isoelectronic traps. These traps are electrically neutral because all four bonds to the neighbouring atoms are satisfied and there is no excess of carrier

present. However, the difference in electronegativity between the impurity and lattice atoms produces a short range potential which binds a primary particle, either an electron or a hole, into a very localized state. The secondary particle is then loosely bound by the screened coulomb potential of the primary particle. A consequence of HTL model is that all the resulting IBE can be classified into isoelectronic acceptors and donors if the secondary particle is a hole or an electron respectively. Furthermore, the excited state spectrum of the loosely bound hole (electron) of an isoelectronic acceptor (donor) should be quite similar to that of an acceptor (donor). This prediction was verified for the even-parity excited state spectrum of IBE bound to N pairs in GaP [53].

Other features of an IBE are its ground state splittings and its very long lifetime. Figure 4-1 shows the energy level diagram of the ground states of an IBE perturbed by a series of interactions. Case (a) corresponds to weak interactions where the "1S" ground state is characterized by the angular momentum of the bound electron and hole $J_e = 1/2$ and $J_h = 3/2$ respectively. In case (b), the ground state is split by coulomb exchange interaction between the electron and hole into an upper $J = 1$ and lower $J = 2$ states. Optical transition from the $J = 1$ state to the crystal ground state is dipole allowed while it is forbidden from the $J = 2$ state. This makes the IBE lifetime at low enough temperature (together

Fig. 4-1

Schematic energy level diagram of the ground states of an IBE under a series of interactions. Case (a) represents the unperturbed "1S" ground state. Case (b) shows the ground state perturbed by electron-hole exchange coupling. The ground state splits into a $J=1$ and $J=2$ state. Case (c) illustrates the effect of an axial crystal field upon the IBE ground states. Only the projection M_J of the total angular momentum along the symmetry axis is conserved. The energy splittings (in units of meV) of the Be-related IBE ground states together with their identifications are shown on the figure.

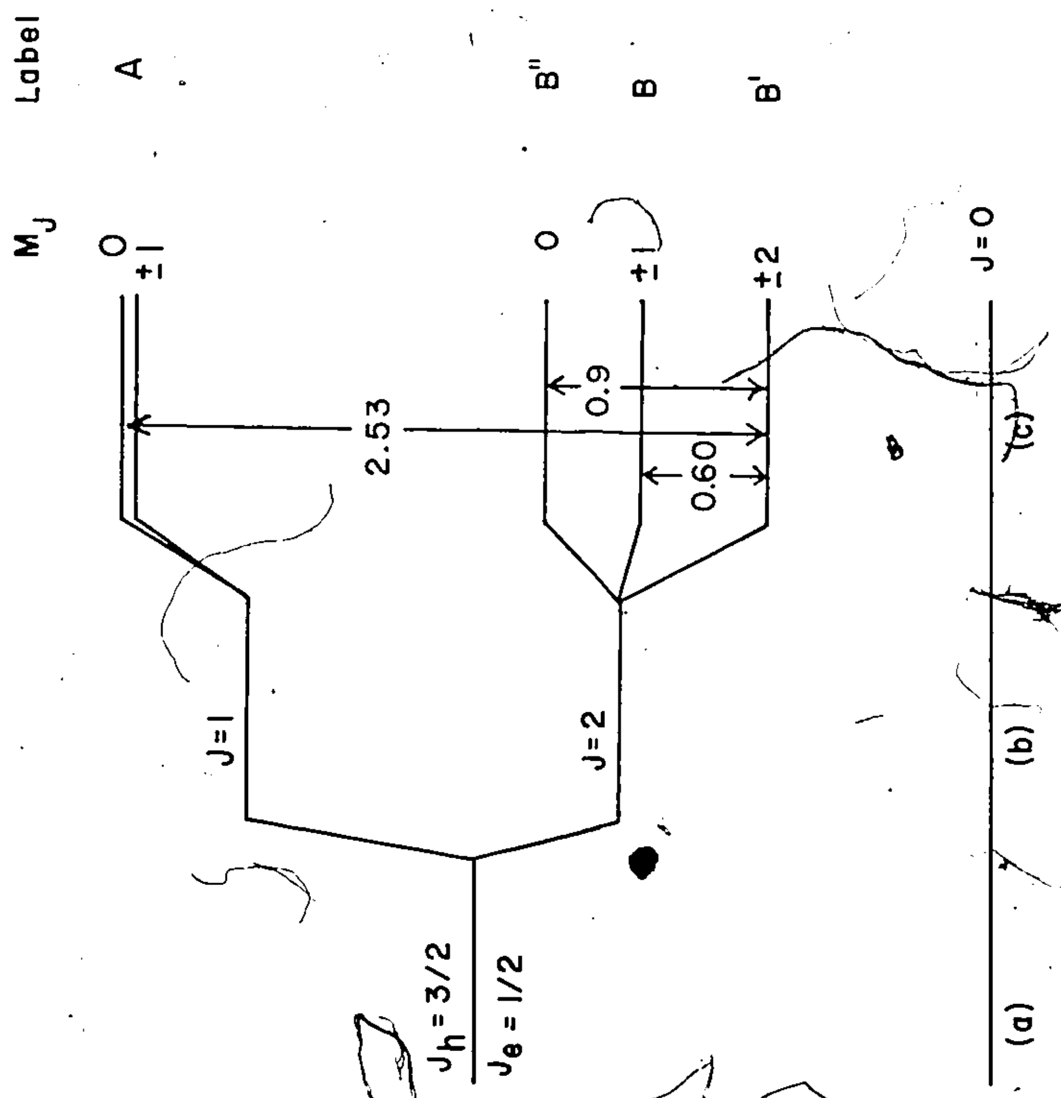

Label
A
B''
B
B'
M_J
0
±1
0
±1
±2
J = 0
2.53
0.9
0.60
J = 1
J = 2
$J_h = 3/2$
$J_e = 1/2$
"1S"
(a)
(b)
(c)

with no Auger recombination process) much longer than any donor or acceptor BE lifetime. Case (c) shows the effect of an axial crystal field upon the IBE ground states. The crystal field can be produced for example by centres with axial symmetry. The split states are labeled by M_J the projection of the total angular momentum along the symmetry axis. The observed energy splittings for the BE-related IBE in silicon together with the assignment of the states are shown in Fig. 4-1. The multiplicity of the even parity ground states results in a temperature dependence of the IBE FIR spectrum. It will be shown in the next section that this temperature dependence will distinguish the IBE FIR spectrum from any typical impurity FIR spectra.

4.3 Experimental Results and Discussion

The experimental results presented in this section were obtained with the same Be-doped samples as those used in previous NIR experiments [51]. The upper curve of Fig. 4-2 shows the transmission spectrum of the sample without correction for instrumental response. The absorption lines α, β γ, and δ are present in the crystal without laser radiation. The line α at 17.2 meV is blended with an absorption line at 17.5 meV due to a Mylar vacuum window in the cryostat. Studies [10] on the electrical and optical properties of Be diffused into high resistivity Si showed that this material is p-type and is composed of several Be acceptor

Fig. 4-2

Uncorrected FIR transmission spectrum of Be-doped Si sample without laser illumination (top), and induced FIR absorption when a Kr^+ laser was incident on the sample (bottom). The lower curve has been shifted up for clarity.

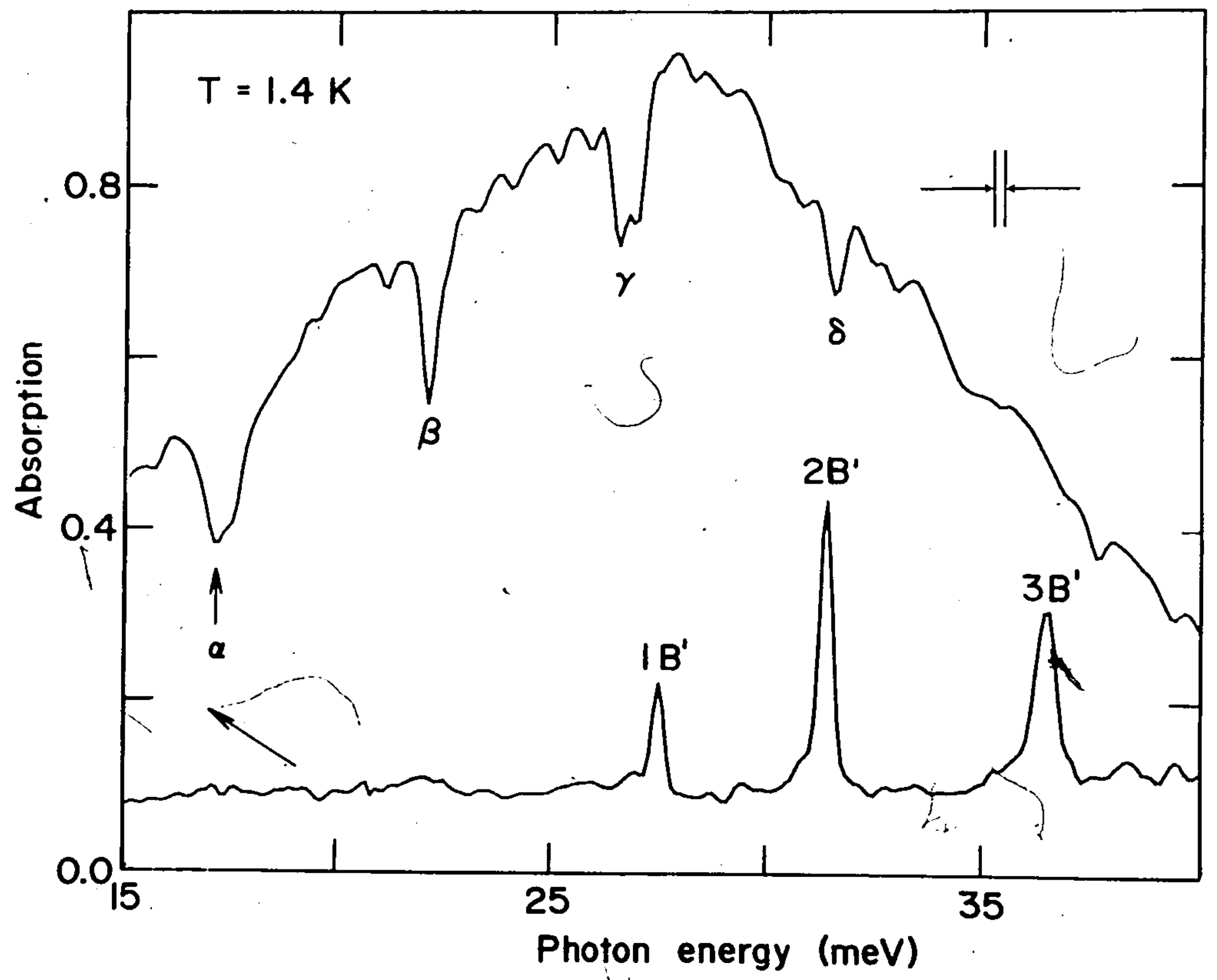

T = 1.4 K
α
β
γ
δ
1B'
2B'
3B'
0.0
0.4
0.8
Absorption
15
25
35
Photon energy (meV)

centres. Therefore, α, β, γ, and δ are associated with transitions of acceptor centres. These transitions are attributed with Be centres since they were not identified with any known acceptor spectra in Si. The relative intensities and energy separations of α, β, and γ are similar to those of a typical shallow acceptor centre in silicon. A comparison between the line positions of this group of lines and effective mass theory [54] provides an estimate of 32.5 meV for the ionization potential of this centre. Using the conductivity sum rule [55] and an effective mass $m^* = 0.4$, the concentration of the acceptor centre is 4.0×10^{13} cm^{-3}.

The lower curve of Fig. 4-2 shows the induced FIR absorption spectrum with incident laser power of 60 mW on the sample. Three induced lines called 1B', 2B', and 3B' are observed. The induced line 2B' is close to the acceptor line δ but the difference in line positions is outside the range of experimental errors. Using the conductivity sum rule with the assumption of an effective mass $m^* = 0.4$, the areal concentration of the centre associated with the induced lines is 4.0×10^{12} cm^{-2}. The excitation depth has not been determined but it is much smaller than the crystal thickness.

Figure 4-3 shows the induced absorption spectrum at 1.4 K, 8 K, and 15 K. At 8 K, new induced absorption lines called 1B, 2B, and 3B are seen on the low energy side of

Fig. 4-3

Temperature dependence of the induced absorption spectrum. The spectra are shifted up for clarity. The three brackets above the absorption lines show the predicted line positions of transitions from the B, B", and A ground state levels based upon the observed line positions of transitions from the B' initial state observed at 1.4 K. The dotted spectrum at the bottom (taken from [56]) shows the FIR absorption spectrum of the boron acceptor shifted down by 3.0 meV.

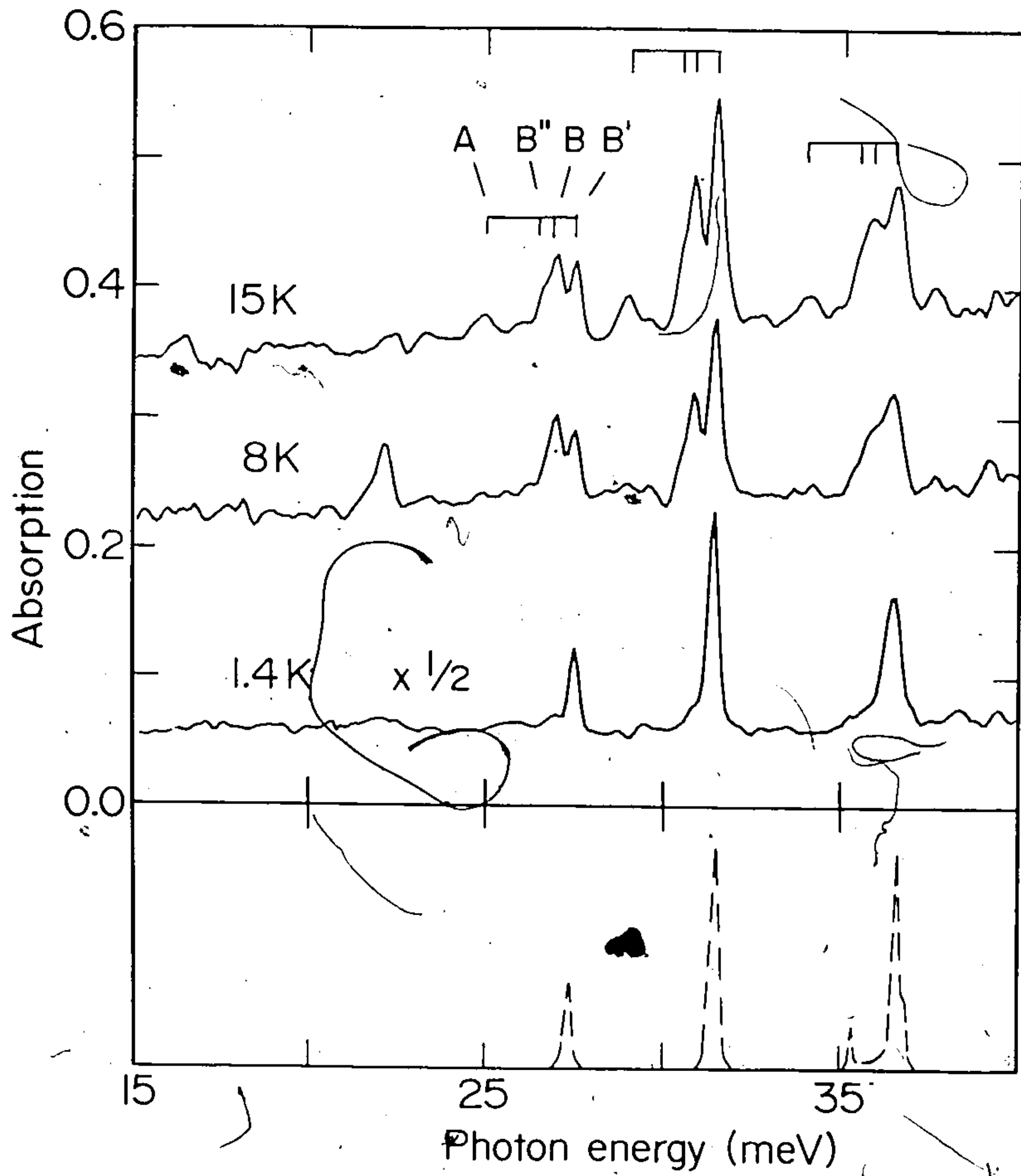

0.6
0.4
0.2
0.0
Absorption
A
B" B B'
15K
8K
1.4K
x 1/2
15
25
35
Photon energy (meV)

1B', 2B', and 3B', each displaced by 0.62 meV from its B' line. An isolated induced line is also observed at 22.13 meV. At 15 K, three additional induced lines 1A, 2A, and 3A are resolved above the noise level and each is separated from its B' component by 2.50 meV.

The induced absorption spectra can be interpreted in terms of IBE transitions associated with the same Be-related IBE as those studied by Thewalt et al. [51]. Figure 4-4 shows a comparison between the IBE energy level structure as determined from NIR measurements and the line positions of the induced FIR absorption lines. As explained in the previous section, the IBE ground state is split into four levels B', B, B", and A which serve as the initial states of the FIR transitions. At 1.4 K, only the lowest B' ground state is populated which results in FIR transitions to the three odd parity excited states (1, 2, and 3). As the temperature increases, the upper B and A ground states become successively populated and FIR transitions from these states are observed.

As shown in Table 4-1, the FIR splittings are in good agreement with those determined from NIR photoluminescence. In addition to the well resolved absorption lines, the 8 K and 15 K spectra reveal a shoulder displaced 0.3 - 0.4 meV below each B line. This new state is in excellent agreement with the predicted [50] zero-field location of the B" state.

Fig. 4-4

Comparison of transitions determined by NIR and FIR spectroscopy. The lowest IBE ground state, B', is taken as the zero of energy. Except for the crystal ground state, all energies (in units of meV) are to scale. The s, m, and w on the NIR excited-state transitions stand for strong, medium, and weak transitions. The symmetry labels on the excited states are those derived in the text from a comparison with acceptor spectra.

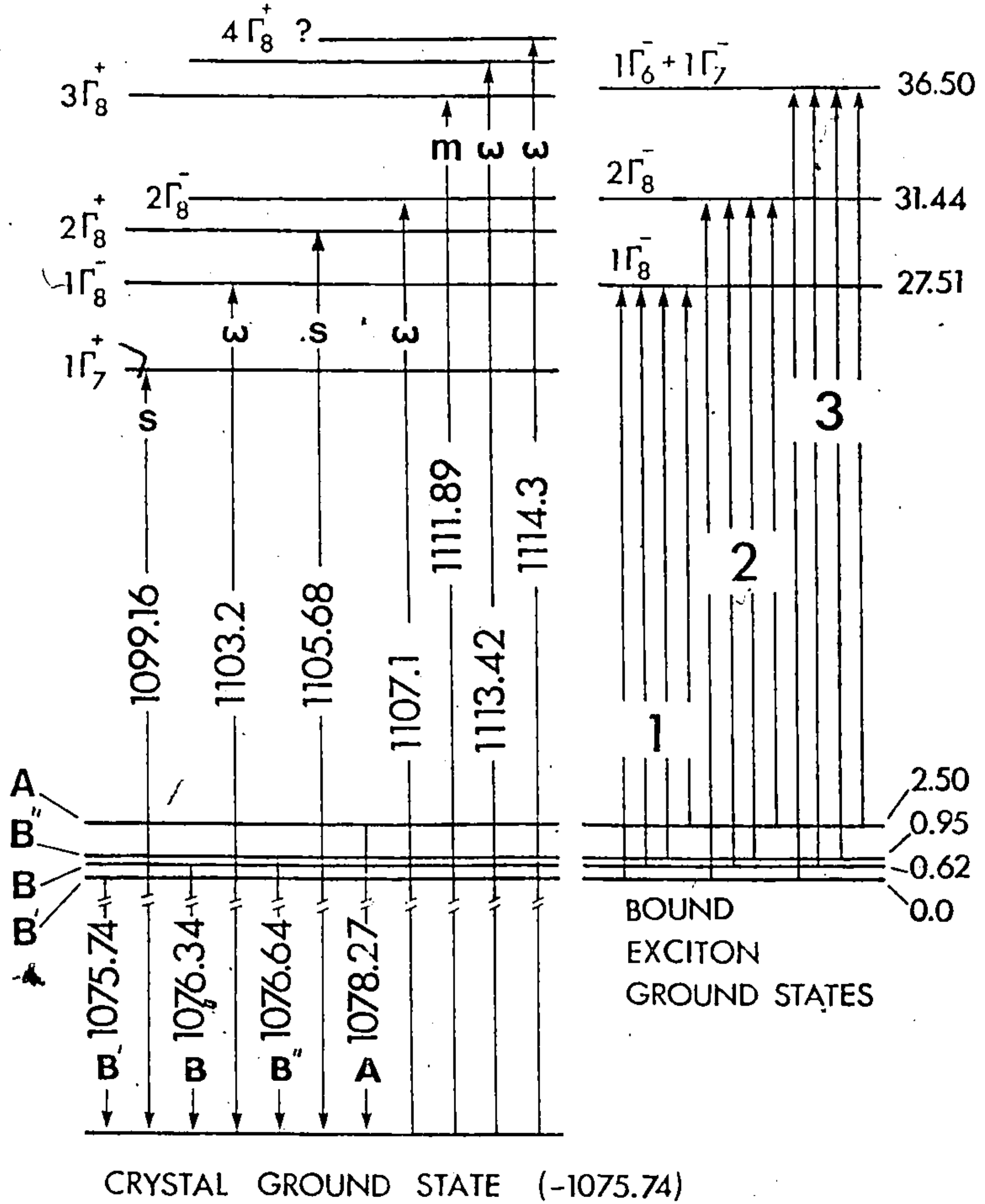
NIR SPECTROSCOPY
FIR SPECTROSCOPY
$4\Gamma_8^+$?
$3\Gamma_8^+$
$2\Gamma_8^-$
$2\Gamma_8^+$
$1\Gamma_8^-$
$1\Gamma_7^+$
$1\Gamma_6^- + 1\Gamma_7^-$
36.50
31.44
27.51
m ω ω
ω s ω
s
1099.16
1103.2
1105.68
1107.1
1111.89
1113.42
1114.3
1
2
3
A
B''
B
B'
2.50
0.95
0.62
0.0
BOUND
EXCITON
GROUND STATES
1075.74
1076.34
1076.64
1078.27
B'
B
B''
A
CRYSTAL GROUND STATE (-1075.74)

Table 4-1

Comparison of energy level differences as determined by NIR and FIR spectra

Assignment	NIR Splitting (meV)	FIR Splitting (meV)
B'-B	0.60±0.10[a]	0.62±0.08
B'-B"	0.9[b]	0.95±0.10
B'-A	2.53±0.13[a]	2.50±0.10
B'-1	27.46±0.20[a]	27.51±0.03
B'-2	31.36±0.20[a]	31.44±0.03
B'-3	---	36.50±0.04

[a] Ref. 51.

[b] Ref. 50.

Further evidence that the FIR and NIR spectra are associated with the same Be centres is provided by the correspondence between the locations of the 1 and 2 excited states with two very weak NIR transitions, as indicated in Fig. 4-4 and Table 4-1. The appearance of these odd parity excited states in the near band edge recombinations spectra shows a partial removal of the selection rules. This partial removal is caused by the low (axial) symmetry of the Be binding centres.

An unexplained feature in the FIR spectra is the absorption line at 22.13±0.04 meV in the 8 K spectrum. This absorption line could be due to a transition from the B ground state to a fourth excited state, but the disappearance of the line at 15 K is unexpected. Therefore this absorption line was not included in the energy level structure of the Be centre.

All of the other observed excited states can be explained within HTL model of an IBE. As illustrated at the bottom of Fig. 4-3, the odd parity excited state spectrum of the shallow acceptor boron [56] shifted to lower energy by 3 meV mirrors the odd parity excited state spectrum of the Be-related IBE in every detail. This direct comparison allows to identify the Be binding centre as an isoelectronic acceptor with a hole binding energy of 43 meV [57]. The IBE 1, 2, and 3 excited states are therefore identified with the acceptor excited states [58] $1\Gamma_8^-$, $2\Gamma_8^-$ and $(1\Gamma_7^- + 1\Gamma_6^-)$.

The identification of the Be binding centre as an isoelectronic acceptor is supported by an interpretation made by Thewalt [59] on the IBE even parity excited states. Figure 4-5 shows a comparison between the even parity excited states of boron acceptor and those of Be-related IBE. The boron $1\Gamma_8^+$ state has been shifted down by 3.0 meV from the IBE lowest ground state. The boron $2\Gamma_8^+$, $3\Gamma_8^+$, and $4\Gamma_8^+$ states [60] are in close correspondence with three IBE energy levels. In particular, the difference in energies between the $2\Gamma_8^+$ state and its associated IBE state is 2.45±0.23 meV, and between the $3\Gamma_8^+$ state and the corresponding IBE state is 3.3±0.23 meV. Both energy differences are in good agreement with the 3.0 meV FIR value, considering that these states are shifted differently by the central cell potential. The weakest $4\Gamma_8^+$ state is in reasonable agreement with a weak IBE state. Finally, the boron $1\Gamma_7^+$ state [61] lying 23.4 meV above the ground state is also observed with the same splitting in the IBE level structure. This splitting was shown [58] to be independent of central cell potentials which produce significant shift of the ground state.

The excellent agreement between the Be-related IBE and boron acceptor quantum structures provides strong evidence for the isoelectronic acceptor assignment of the Be binding centre. Previous studies [9,50-51] were based on an isoelectronic donor model. The motivation for using

Fig. 4-5

Comparison between the even parity excited states of boron acceptor with those of IBE. The boron ground state was shifted down by 3.0 meV with respect to the IBE lowest ground state. All energies (in units of meV) are to scale. The labels on the excited states are explained in Fig. 4-4.

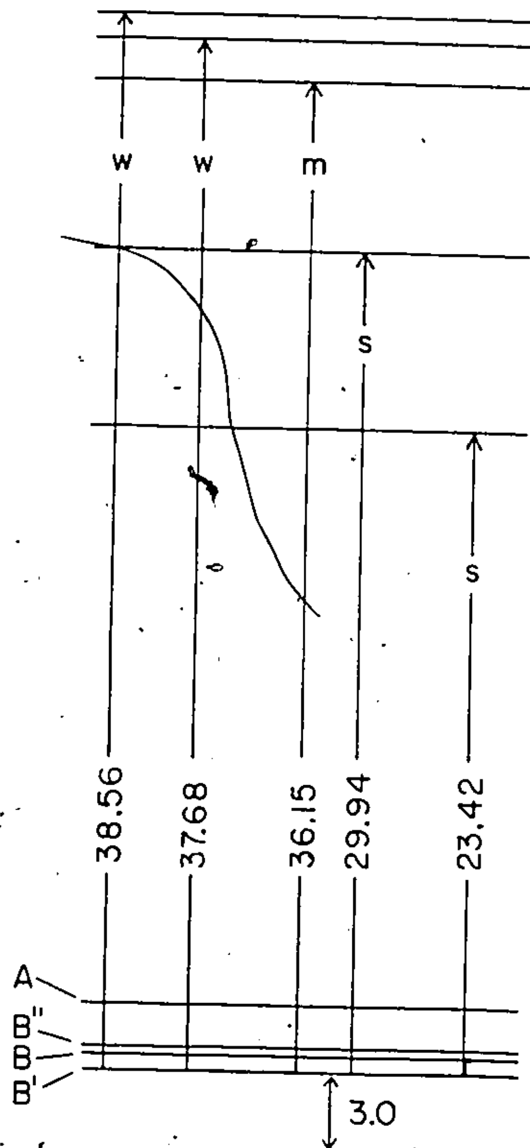

Be-related
Isoelectronic Bound
Exciton
w
w
m
s
s
38.56
37.68
36.15
29.94
23.42
A
B''
B
B'
3.0

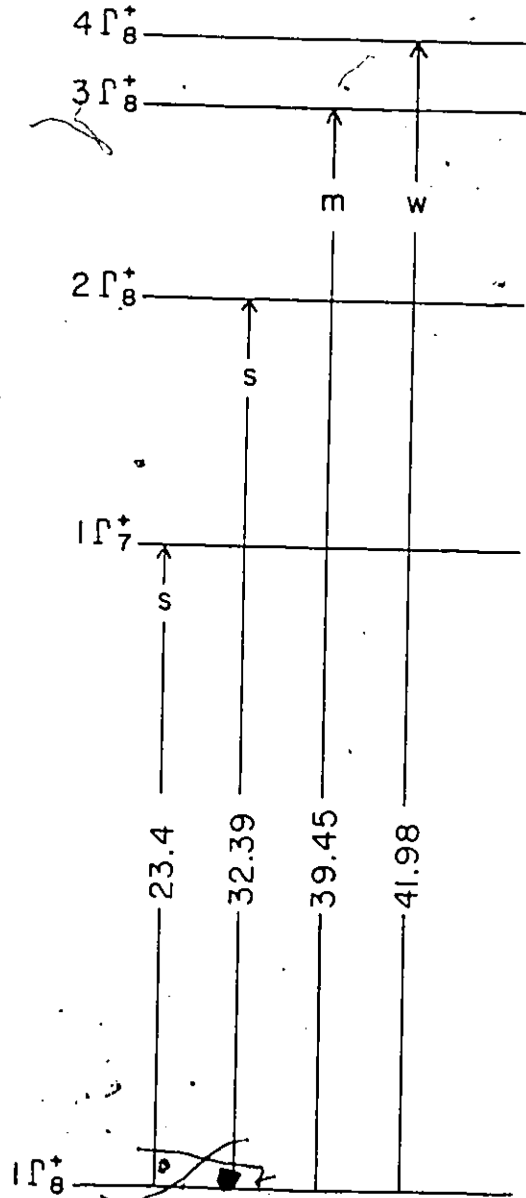

Boron
Acceptor
$4\Gamma_8^+$
$3\Gamma_8^+$
m
w
$2\Gamma_8^+$
s
$1\Gamma_7^+$
s
23.4
32.39
39.45
41.98
$1\Gamma_8^+$

this model lay in the interpretation of the IBE phonon sidebands which provide information on the IBE primary particle. The interpretation of the IBE FIR spectra, unlike their phonon sidebands, is very simple. It reveals the nature of the isoelectronic binding centre and provides the binding energy of the secondary particle.

In conclusion, the first FIR absorption spectrum of a bound exciton was reported and was shown to be an important tool for the interpretation of the BE quantum structure. The energy level structure of the Be-related IBE was identified with known acceptor excited states and was found to have a hole binding energy of 43 meV. This technique should be applicable to many other BE systems in silicon and in other semiconductors. In particular, it could provide some information about the nature of the short range potential which binds an exciton.

CHAPTER 5

DIRECT DETERMINATION OF THE EQUILIBRIUM CONSTANT OF THE EXCITON-CARRIER GAS IN GERMANIUM

5.1 Introduction

The low density exciton-carrier gas in germanium is a simple system that can be used to investigate the thermal behaviour of nonequilibrium states in a semiconductor. This behaviour may differ from that of a classical gas due to the finite lifetime of excitons and carriers. In the case where lifetime effects are negligible, the concentration of excitons and carriers should obey the law of mass action of a classical gas with an equilibrium constant derived using statistical mechanics. The understanding of the thermal properties of this system is also essential to the study of the metal-insulator transition of the gas at high carrier densities.

The ionization process of the exciton-carrier gas was studied by using several methods. Timusk [62] observed a thermal dissociation of the exciton gas in germanium by using the FIR absorption associated with excitons. He explained his results with a kinetic model including a temperature dependent ionization rate of excitons. Mock et al. [63] observed a quadratic decrease of the exciton luminescence with decreasing carrier generation rate at constant temperature. Their results showed the expected behaviour of the dissociation of excitons, in thermal equili-

brium with carriers, as a function of carrier generation rate. A more detailed study was done in silicon by Gourley and Wolfe [64]. From their steady-state and time-resolved luminescence data, they extracted the equilibrium constant of the exciton-carrier gas. These investigations did not provide any information on the free carrier concentration. In particular, the luminescence experiments are mainly sensitive to electron-hole overlap which make them inappropriate to the study of free carriers.

The purpose of this study was to present measurements on both free carrier and exciton concentrations as a function of temperature by using FIR spectroscopy. These measurements were made at concentrations much smaller than (< 4%) the Mott density [65] where the exciton-carrier gas is expected to be nearly ideal. Data on the exciton and carrier concentrations allowed a direct determination of the equilibrium constant for any given temperature and carrier generation rate. The experimental equilibrium constant was found to be in excellent agreement with the classical equilibrium constant of an ideal gas.

In the next section, the method of calculation of the FIR absorption spectrum associated with free carriers is presented. The method will be used in section 5.3 to decompose the measured FIR absorption into free carrier and exciton absorptions. Their absorption strengths will be employed to estimate the concentration of each species. The

experimental equilibrium constants obtained at several temperatures will be compared to the predicted temperature dependent equilibrium constant of an ideal gas.

5.2 Far-Infrared Absorption Spectrum of Free Carriers in Germanium

The absorption coefficient of free carriers can be written as

$$\alpha(\omega) = \frac{\omega}{c\varepsilon_o^{\frac{1}{2}}} \operatorname{Im}[\varepsilon(\omega)] \tag{5-1}$$

where c is the speed of light, ε_o is the static dielectric constant of Ge, and $\varepsilon(\omega)$ is the dynamic dielectric constant of an electron-hole plasma in Ge. The dynamic dielectric constant was studied by several workers [66-68]. It was found that $\bar{\varepsilon}(\omega) = \varepsilon(\omega)/\varepsilon_o$ was composed of two contributions

$$\bar{\varepsilon}(\omega) = \varepsilon_{intra}(\omega) + \varepsilon_{inter}(\omega) . \tag{5-2}$$

The intraband contribution to the dielectric constant $\varepsilon_{intra}(\omega)$ is due to damped plasma oscillations of electrons and holes in which the carriers remain in the same band. It is given by

$$\varepsilon_{intra}(\omega) = 1 - \frac{\omega_p^2}{\omega(\omega+i\Gamma_D)} , \tag{5-3}$$

where

$$\omega_p^2 = \frac{4\pi e^2}{\varepsilon_o} \left(\frac{n}{m_{oe}} + \frac{n_L}{m_{oL}} + \frac{n_H}{m_{oH}}\right) . \qquad (5\text{-}4)$$

$n = n_L + n_H$ is the electron-hole pair (or free carrier) density, n_L and n_H are the light and heavy hole densities respectively. m_{oL} and m_{oH} are the optical masses of light and heavy holes, and Γ_D is the Drude damping constant which is defined as the inverse of the collision (or "relaxation") time.

The interband contribution to the dielectric constant $\varepsilon_{inter}(\omega)$ is due to hole transitions from the heavy (light) to light (heavy) hole bands assisted by the absorption (emission) of photons. $\varepsilon_{inter}(\omega)$ in the random phase approximation is

$$\varepsilon_{inter}(\omega) = 4\pi e^2 \int_0^\infty dE \, \frac{E}{E^2 - \omega(\omega + i\Gamma_I)} \, N(E) , \qquad (5\text{-}5)$$

where

$$N(E) = \sum_{\underline{k}} \delta(E - (E_L(\underline{k}) - E_H(\underline{k}))) f_H(\underline{k}) \times (1 - f_L(\underline{k})) \left[\lim_{q \to 0} \frac{|\rho^{HL}_{\underline{k},\underline{k}+\underline{q}}|^2}{q^2}\right] . \qquad (5\text{-}6)$$

e is the electron charge, Γ_I is the interband damping constant, N(E) is defined as the optical density of states of holes, $f(\underline{k})$ are Fermi distribution functions, $E_{H,L}(\underline{k})$ are the energy dispersion of the valence band edge given by eq. (3-1).

and the term in square brackets on the right hand side of eq. (5-6) is the interband transition matrix element [66].

A computer program [69] was used to evaluate eqs. (5-1) to (5-6) in the frequency range from 0.2 meV to 20 meV. Since Γ_I was smaller than the integration step employed in eq. (5-5), the following approximation

$$\lim_{\Gamma_I \to 0} \mathrm{Im}[\varepsilon_{inter}(\omega)] = 2\pi^2 e^2 N(\omega) \qquad (5\text{-}7)$$

was utilized in eq. (5-1).

Figure 5-1 shows an example of a calculated FIR absorption spectrum of free carriers together with the intraband and interband contributions to the total absorption. The dashed line shows the intraband contribution α_{intra} to the absorption coefficient. It increases abruptly at low frequencies while it decreases as ω^{-2} at high frequencies. The ω^{-2} dependence at frequencies greater than 5 meV makes α_{intra} very small. The double dashed curve (— --) represents the interband contribution α_{inter} to the absorption coefficient. α_{inter} exhibits a maximum at $\sim$ 3 meV and decreases smoothly at higher frequencies. The total absorption coefficient (——) displays the behaviour of α_{intra} at low frequencies while it follows that of α_{inter} at high frequencies. These two distinct behaviours make possible a direct determination of the Drude damping constant and free carrier density.

Fig. 5-1

Theoretical FIR absorption spectrum of free carriers. All the parameters used in the calculations of this spectrum are shown on the figure and in Table 3-1. The intraband (—— -) and interband (—— --) contributions to the total absorption coefficient (———) are also shown. The total absorption coefficient closely follows α_{intra} at low frequencies while it follows α_{inter} at high frequencies. The fine structure on the curve is due to finite number of points used to evaluate eq. (5-6).

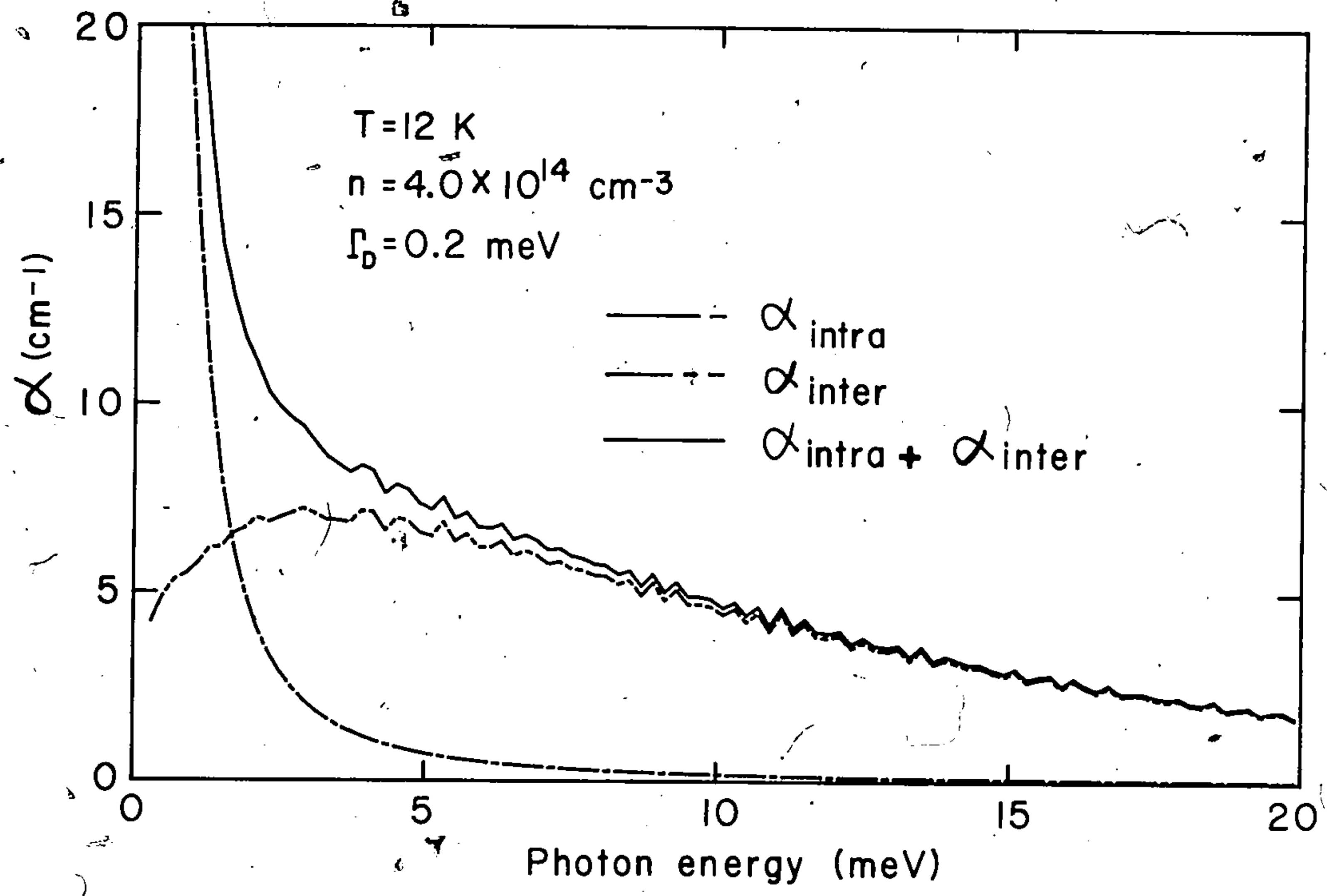

T=12 K
n=4.0×10^14 cm-3
Γ_D=0.2 meV
α intra
α inter
α intra + α inter
Photon energy (meV)
α (cm-1)
0
5
10
15
20

Figure 5-2 shows α_{intra} at three values of the Drude damping constant Γ_D. As Γ_D increases, the strong absorption edge shifts to higher frequencies while α_{intra} still remains small at high frequencies. This makes the absorption spectrum of free carriers at low frequencies very sensitive to Γ_D.

Figure 5-3 shows α_{inter} at a free carrier density of 8.0×10^{14} cm^{-3} and at three representative temperatures. At 6.5 K, most of the interband absorption is located below 5 meV. Above 5 meV, α_{inter} decreases in an exponential fashion. As the temperature increases, the maximum of α_{inter} decreases in amplitude and shifts to higher frequencies such that at 34 K α_{inter} becomes almost constant in the spectral region from 5 meV to 20 meV. The flattening of α_{inter} with increasing temperature is due to holes which are thermally excited into higher energy states of the heavy hole band. These heavy holes then make absorption of higher energy photons more probable.

Calculations done at several carrier densities and temperatures show that α_{inter} can be approximated as

$$\alpha_{inter}(\omega,n,T) = nf(\omega,T) \qquad (5\text{-}8)$$

where 10^{14} cm^{-3} $< n < 10^{15}$ cm^{-3} and $f(\omega,T)$ is a function of frequency and temperature. Equation (5-8) indicates that the frequency dependence of α_{inter} is determined by the temperature only and the overall shape of α_{inter} scales with

Fig. 5-2

Theoretical intraband contribution to the free carrier absorption coefficient at several values of the Drude damping constant. The parameters used in the evaluation of α_{intra} are shown on the figure and in Table 3-1.

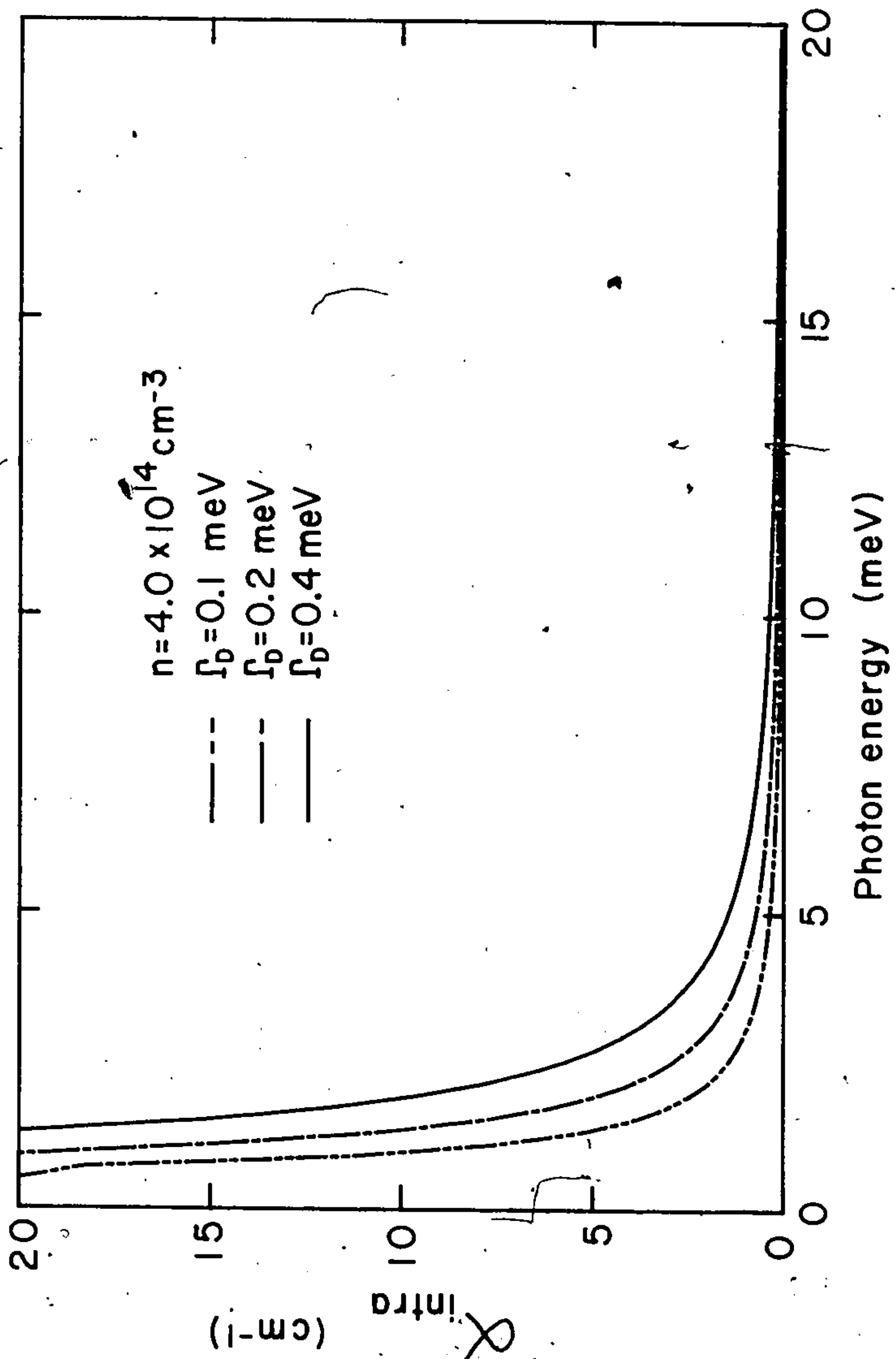

n=4.0 x 10^14 cm-3
Γ_D=0.1 meV
Γ_D=0.2 meV
Γ_D=0.4 meV
Photon energy (meV)
α_intra (cm-1)
0
5
10
15
20

Fig. 5-3

Calculated interband contribution to the free carrier absorption coefficient at 6.5 K, 12 K, and 34 K. Notice the flattening of α_{inter} as the temperature increases.

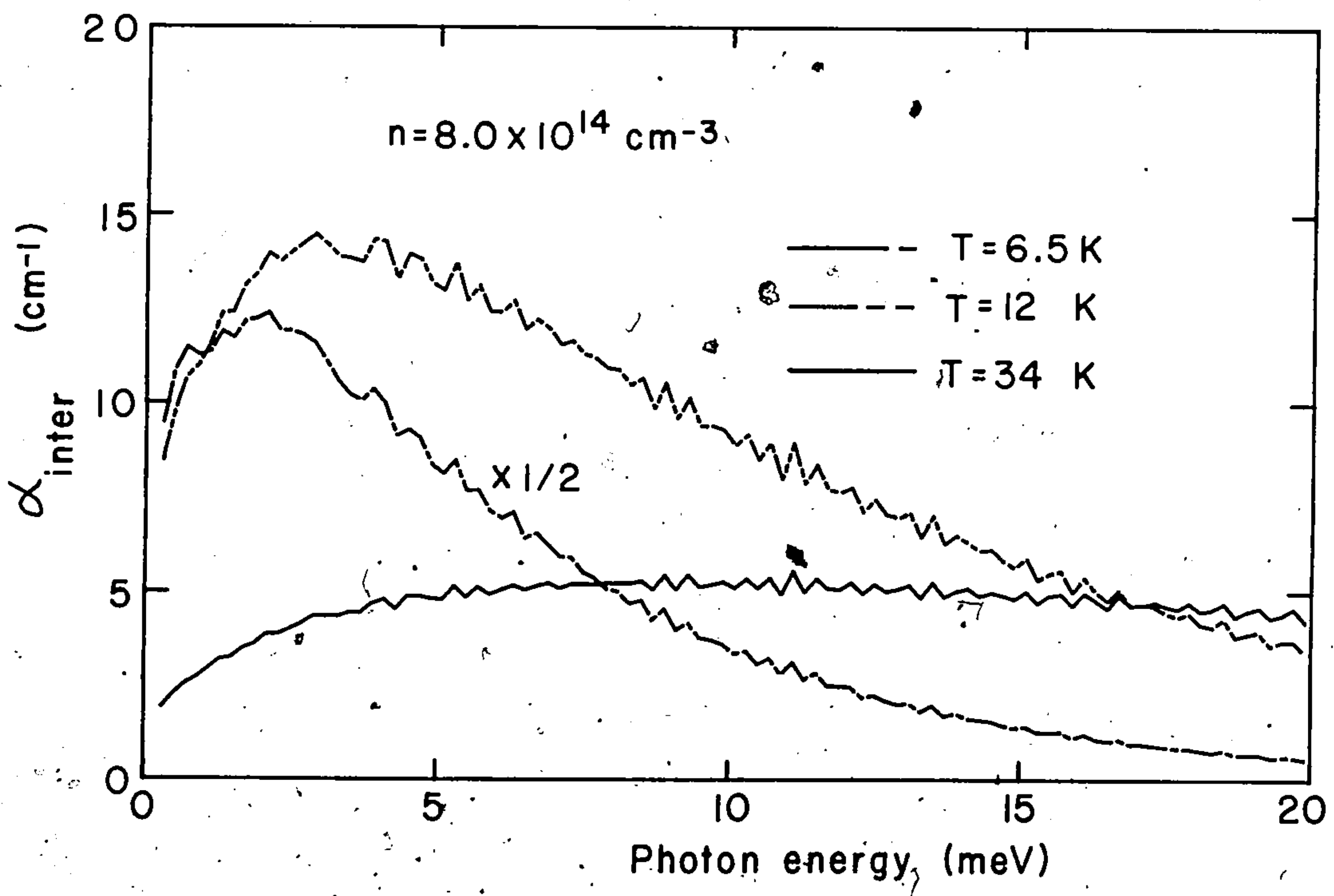

n=8.0×10^14 cm-3
T=6.5 K
T=12 K
T=34 K
×1/2
α inter (cm-1)
0
5
10
15
20
Photon energy (meV)

electron-hole pair density. This important feature will be used in the next section to determine the free carrier density.

5.3 Thermodynamics of Exciton-Carrier Gas in Germanium

The experiments were carried out with two Ge samples. A 0.37 mm thick sample was used at temperatures lower than 20 K to obtain good spatial uniformity of excitons and free carriers [70]. However a 3 mm thick sample was used at 34 K to get an observable absorption at high frequencies.

The temperature dependence of the total absorption of free carriers and excitons is shown in Fig. 5-4. The spectra were taken at the same laser power. At 7.3 K the total absorption is dominated by excitons with two strong lines at 3.0 meV and 3.4 meV and a weaker line at 2.4 meV. There is also a continuum of absorption starting at 4.1 meV. The absorption lines and the continuum are associated with the 1S-2P transitions [30] and with transitions from the 1S ground states to the continuum of excitons [27,71], respectively. As the temperature increases, the two strong lines decrease in strength showing a thermal ionization of excitons and a continuous absorption develops below $\sim$ 2.4 meV. The continuous absorption was initially interpreted by Timusk [62] as produced by a plasma of free electrons and holes in thermal equilibrium with excitons. The spectra shown in Fig. 5-4 suffer from Fabry-Perot interference

Fig. 5-4

Temperature dependence of the absorption of free carriers and excitons at constant laser power. Notice the decrease in strength of the exciton absorption lines and the increase in absorption at low photon energy as the temperature increases. The oscillations in the spectra are due to Fabry-Perot interference fringes caused by the parallel faces of the thin sample.

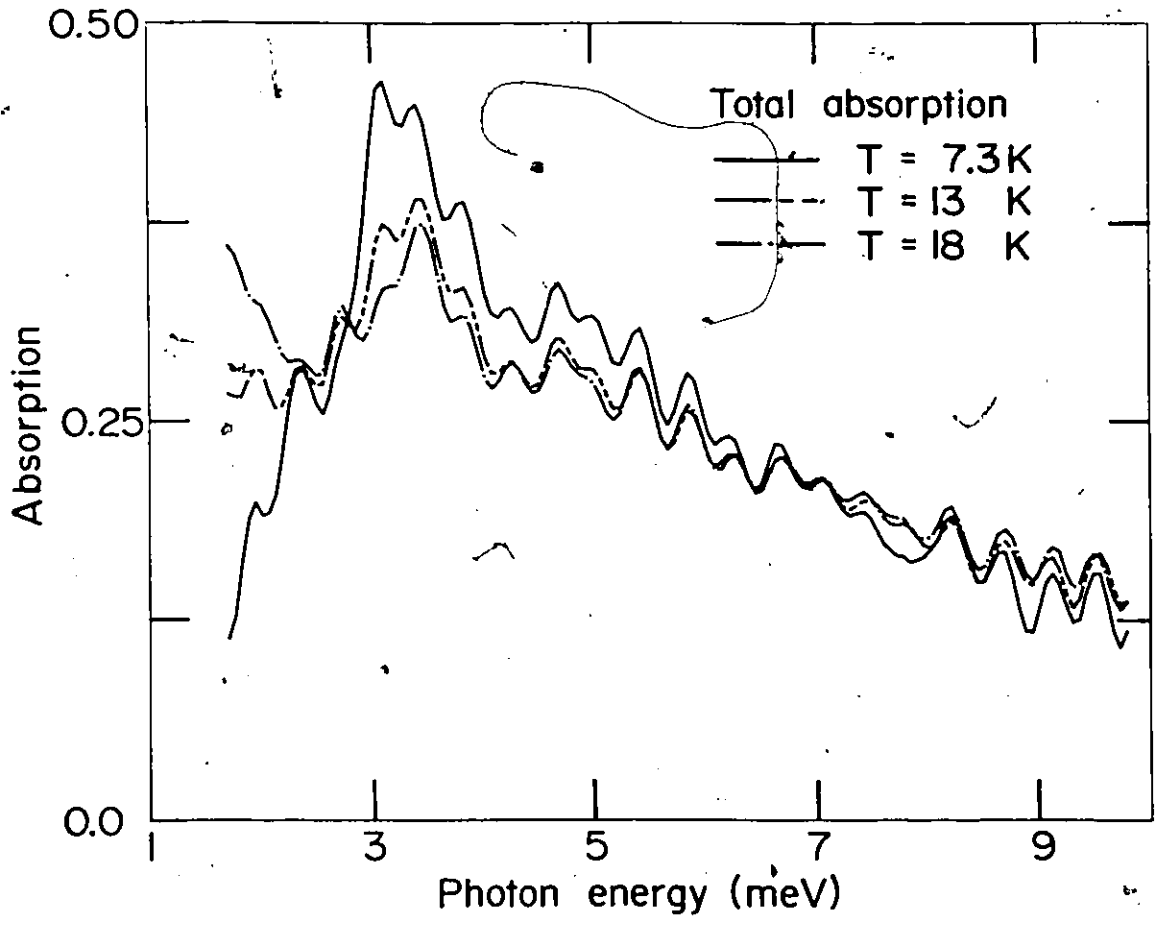
Total absorption
T = 7.3K
T = 13 K
T = 18 K
Absorption
0.50
0.25
0.0
1
3
5
7
9
Photon energy (meV)

fringes caused by the parallel faces of the thin sample.

These results can be understood by considering the thermal equilibrium between free carriers and excitons. The equation governing their concentrations is [72]

$$\frac{n_c^2}{n_x} = n^* = \frac{g_e g_h}{g_x} \left[\frac{m^* kT}{2\pi\hbar^2}\right]^{3/2} e^{-E_x/kT} \qquad T > 5K \qquad (5\text{-}9)$$

where n_c and n_x are the concentration of free carriers and excitons respectively, g_i and m_{di} are the degeneracy factor and the density of states masse of particle i respectively, $m^* = m_{de}m_{dh}/m_{dx}$ and E_x is the binding energy of excitons. Here we have neglected the contribution to n^* coming from the finite lifetime of excitons. Assuming that the degeneracies cancel and the heavy holes predominate, the equilibrium constant n^* becomes [73]

$$n^* = 2.66\times10^{14}\ T^{3/2}e^{-48/T}\ cm^{-3}\ . \qquad (5\text{-}10)$$

The exciton concentration was evaluated from Timusk's procedure by using the total absorption associated with excitons and an absorption length of 0.37 mm or 1 mm corresponding to a sample thickness of 0.37 mm or 3 mm respectively. The exciton concentration is given by [74]

$$n_x = 9.0\times10^{13}\ \langle \ell n(I_0/I)\rangle/D \qquad (5\text{-}11)$$

where $\langle \ell n(I_0/I)\rangle$ is the exciton absorption averaged over the

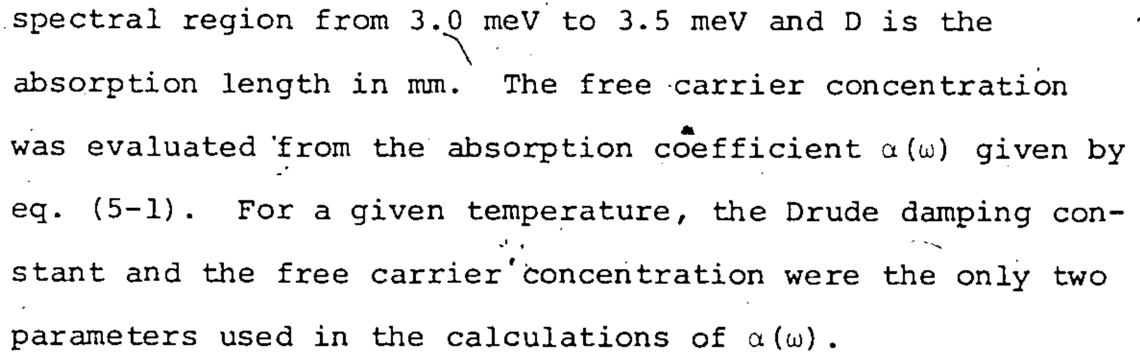

spectral region from 3.0 meV to 3.5 meV and D is the absorption length in mm. The free carrier concentration was evaluated from the absorption coefficient $\alpha(\omega)$ given by eq. (5-1). For a given temperature, the Drude damping constant and the free carrier concentration were the only two parameters used in the calculations of $\alpha(\omega)$.

An example of decomposition of the measured absorption into free carrier and exciton absorption is shown in Fig. 5-5. The upper curve of Fig. 5-5a shows the total absorption taken at 18 K. Also shown is the calculated absorption of free carriers. The free carrier absorption length used in the calculations was the same as that of excitons. The rise in absorption at photon energy less than 3 meV is associated with the Drude absorption of a collection of classical charged particles with a given damping rate Γ_D. The nearly constant absorption observed at higher photon energy is caused by transitions of holes from the heavy to light hole valence bands. Figure 5-5b shows a comparison between the exciton spectrum taken at 7.3 K and at 18 K. The 18 K spectrum was obtained by subtracting the calculated free carrier absorption from the measured absorption. A small correction was made to the 7.3 K spectrum due to a residual absorption ($\sim$ 0.01) of free carriers [75]. Except for the small temperature dependence of the absorption lines, good agreement is observed between the two spectra. Furthermore, the fitted Drude damping

Fig. 5-5

Decomposition of the total absorption into free carrier and exciton absorptions. Figure 5-5a shows the measured (solid line) absorption spectrum and the calculated (dashed line) free carrier absorption. Figure 5-5b shows a comparison between the exciton spectrum (solid line) taken at 7.3 K and the spectrum (dashed line) obtained by subtracting the calculated free carrier absorption from the total absorption.

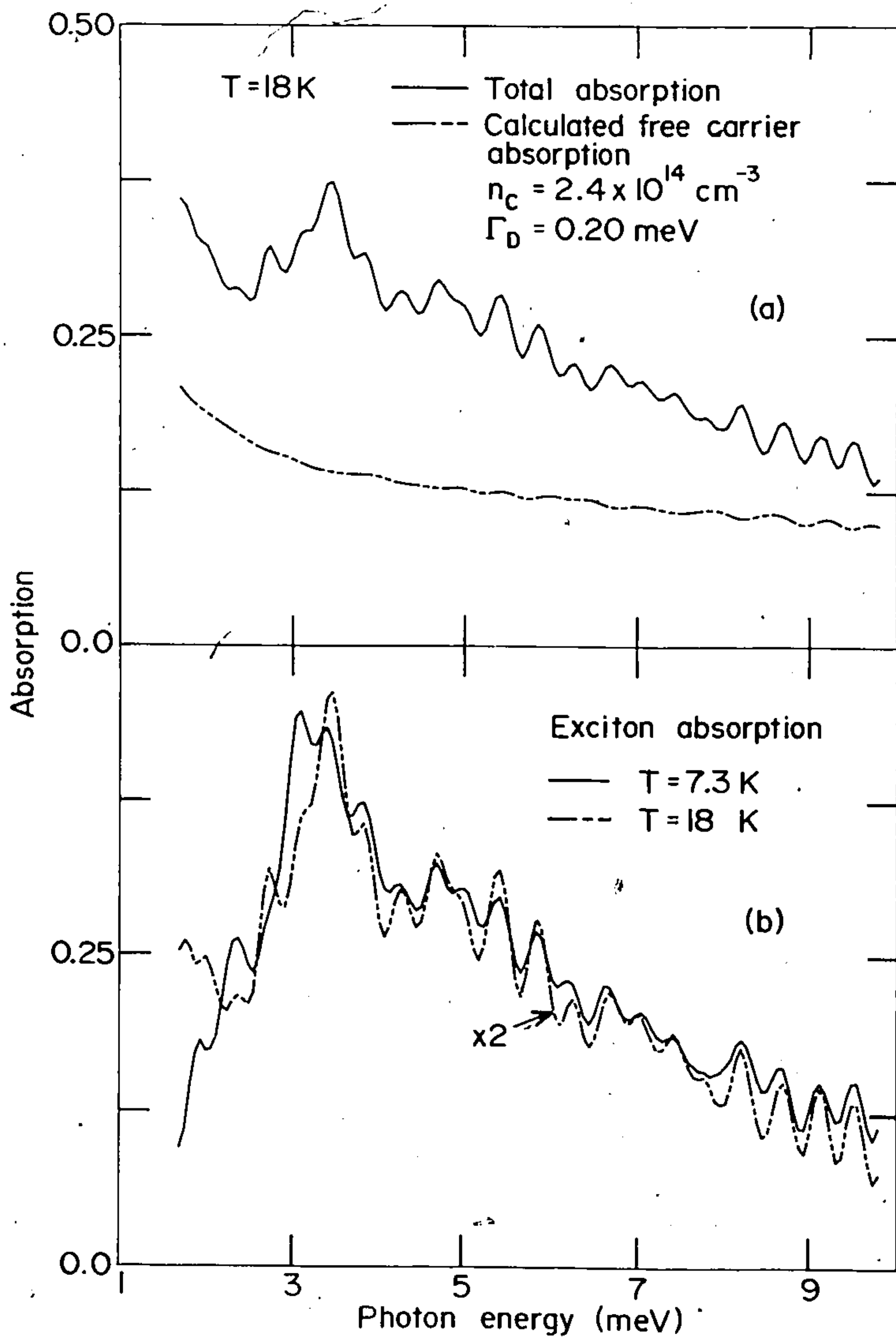

0.50
0.25
0.0
0.25
0.0
T = 18 K
Total absorption
Calculated free carrier absorption
$n_c = 2.4 \times 10^{14}\ cm^{-3}$
$\Gamma_D = 0.20$ meV
(a)
Exciton absorption
T = 7.3 K
T = 18 K
(b)
x2
Absorption
1
3
5
7
9
Photon energy (meV)

constant with Γ_D = 0.20±0.03 meV is in excellent agreement with Meyer and Glicksman's result [76] of Γ(21K) = 0.17 meV derived from their DC conductivity measurements made at a free carrier concentration of 2.4×10^{14} cm^{-3}. Our result is also in good agreement with the value Γ(15K) = 0.15 meV as determined by extrapolating the cyclotron resonance data of Kawamura et al. [77] at the same density.

Another example of such a fit is shown in Fig. 5-6. The absorption spectrum was taken at 34 K where most of the excitons are ionized. Also shown is the calculated absorption of free carriers. The residual absorption between the measured and calculated absorption is associated with excitons. Considering this residual absorption the calculated absorption fits the data very well. Again the Drude damping constant derived from the fit Γ_D = 0.23±0.02 meV is in good agreement with Meyer and Glicksman's data Γ(32K) = 0.17 meV at a free carrier concentration of 4.8×10^{14} cm^{-3}. This shows that the free carrier absorption is well described by eq. (4-1) with the dynamic dielectric constant of an electron-hole plasma.

Having determined the free carrier and exciton concentrations from the above procedure, we can evaluate the equilibrium constant as a function of temperature. Figure 5-7 shows a comparison between the measured and calculated equilibrium constants. The solid curve was obtained from eq. (5-10). Good agreement is observed between theory and

Fig. 5-6

High temperature absorption spectrum of excitons and free carriers. At this temperature almost all excitons are ionized producing a residual absorption in the spectrum. Considering this residual absorption the calculated (dashed line) free carrier absorption agrees very well with the low and high energy dependence of the measured spectrum.

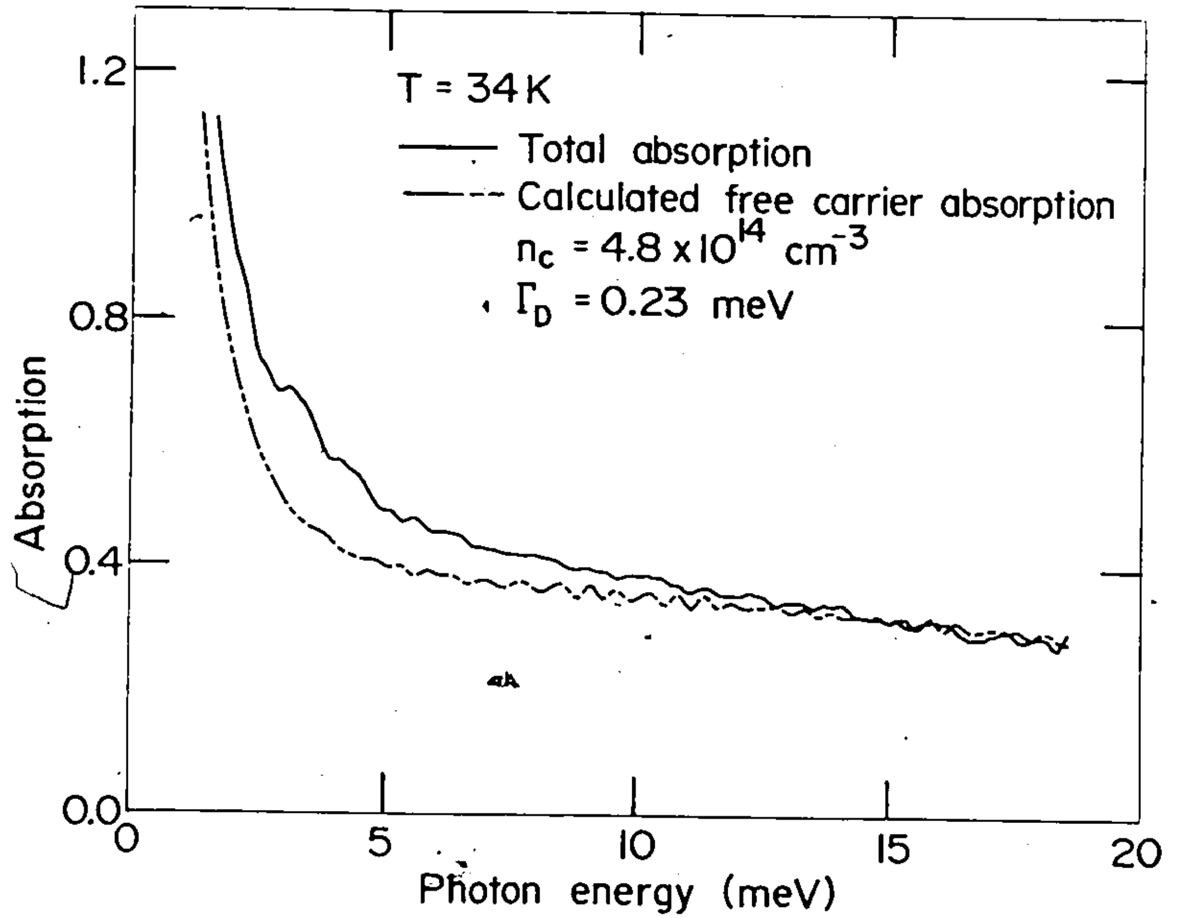
T = 34 K
Total absorption
Calculated free carrier absorption
$n_c = 4.8 \times 10^{14}$ cm^{-3}
$\Gamma_D = 0.23$ meV
Absorption
Photon energy (meV)
0.0
0.4
0.8
1.2
0
5
10
15
20

Fig. 5-7

Thermodynamic equilibrium constant as a function of temperature. The solid curve was derived from eq. (5-10) while the data points were obtained from the measurements of the excitons and free carrier concentrations. The good agreement between theory and experiment shows that the exciton-carrier gas is well described by the thermal equilibrium of an ideal gas.

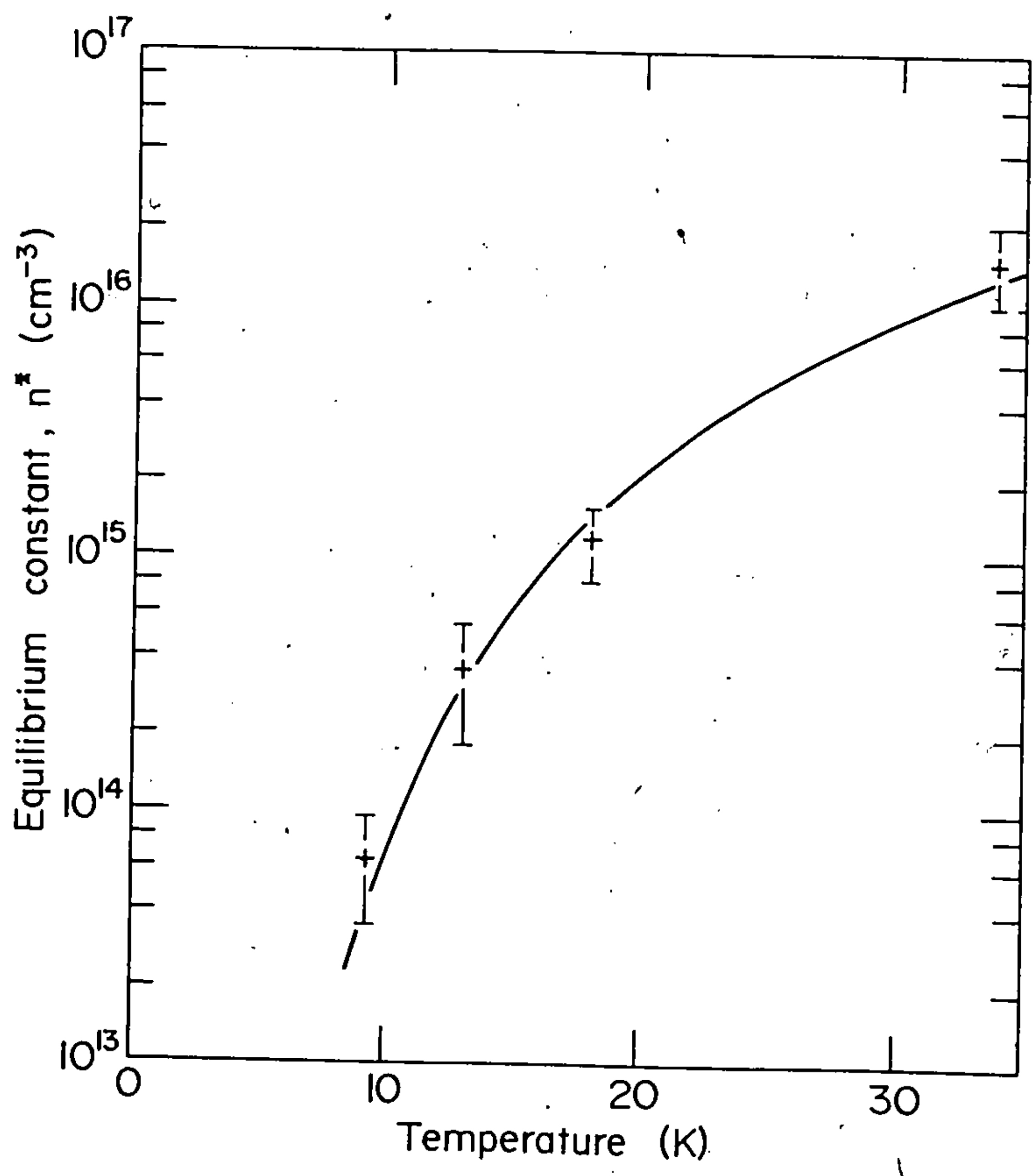
Equilibrium constant, n* (cm⁻³)
10¹⁷
10¹⁶
10¹⁵
10¹⁴
10¹³
0
10
20
30
Temperature (K)

experiment over a wide range of temperatures and concentrations. This demonstrates that the concentration of excitons and carriers obey eq. (5-9) with the equilibrium constant derived by using statistical mechanics. This work can be extended to investigate the ionization process of excitons at high carrier concentration where a lowering of the ionization potential occurs. Previous investigations [78,71] have been done to study the Mott transition of the exciton gas at high carrier density and the associated phase diagram. The experiments were not conclusive and were given conflicting interpretations. Measurements of the exciton and carrier concentrations by using FIR spectroscopy would provide the ionization potential of the exciton gas as a function of carrier concentration. This in turn can be used to obtain direct information on the type of phase diagram of the photoexcited gas.

In summary, for a low enough concentration of electron-hole pairs the total absorption can be separated into absorption by excitons and a low density electron-hole plasma. This makes possible a direct determination of the absolute value of the equilibrium constant as a function of temperature. The good agreement between theory and experiment shows that the free carriers and excitons behave like an ideal gas in thermal equilibrium. This method can also be used to determine the shift of the free carrier continuum

as a function of the free carrier concentration. This would provide a direct method to investigate the nature of the Mott transition at high concentration of electron-hole pairs.

CHAPTER 6

CONCLUSIONS

The aim of this thesis was to study three aspects of exciton physics in germanium and silicon. The results and conclusions of the studies are summarized in this chapter.

In the first part of this thesis, the energy level structure of free excitons was investigated in stressed germanium. At high stress, the FIR absorption spectrum of free excitons is very simple and consists of strong, isolated absorption lines. This simple FIR spectrum results from the formation of excitons with electrons in the lowest conduction band minimum and holes in the upper valence band maximum. Both bands have constant energy surfaces described by ellipsoids of revolution with the symmetry axis along the stress axis. A theoretical model was used to predict the locations and linestrengths of transitions. Good agreement was obtained between experiment and theory. In contrast to the zero stress case, in the high stress limit every observed transition was accounted for theoretically and every predicted transition was observed experimentally. It was found that at high stress the quantum structure of free excitons is nearly hydrogen-like and, hence, supports the close analogy between free excitons and hydrogen atoms.

In the second part of this thesis, the first FIR absorption spectrum of a bound exciton was presented. The FIR spectrum of the Be-related isoelectronic bound exciton together with previous results on its even parity excited states were shown to be in excellent agreement with known boron acceptor excited states. The results shown in this thesis present the cleanest demonstration of the validity of the isoelectronic acceptor/donor model of the energy level structure of deep isoelectronic binding centres. The FIR technique can also be applied to shallower isoelectronic binding centres like nitrogen pairs in GaP, where the IBE internal structure is neither that of an acceptor (or donor) nor that of a weakly perturbed exciton. The FIR spectra of these centres would provide physical insights into the central cell potential of the defect which binds an exciton.

In the last part of this thesis, the thermodynamic equilibrium between free excitons and carriers was investigated in Ge by using FIR spectroscopy. It was shown that the FIR technique is a sensitive probe of free carriers and provides information on the absolute concentration of free carriers and excitons. In particular, it was found that the theoretical absorption coefficient of free carriers given by eq. (5-1) with the dynamic dielectric function of an electron-hole plasma in Ge is in excellent agreement with the experimental data. The concentrations of excitons and free carriers were found to obey the Saha equation of an ideal gas

in thermal equilibrium. This study can be extended to investigate the ionization potential of excitons at high carrier densities where the exciton-carrier gas is strongly interacting.

APPENDIX A

EVALUATION OF THE ENERGY LEVELS OF EXCITONS

In cylindrical coordinates, the exciton Hamiltonian for the relative motion is (3-9)

$$-H_r(\gamma) = [\frac{\partial^2}{\partial\rho^2} + \frac{1}{\rho}\frac{\partial}{\partial\rho} + \frac{1}{\rho^2}\frac{\partial^2}{\partial\phi^2} + \frac{\partial^2}{\partial z^2}] + \frac{2}{(\rho^2+z^2)^{\frac{1}{2}}} \quad \text{(A-1)}$$

The Rayleigh-Ritz method was used to solve the eigenvalue equation $H_r|\psi_n\rangle = E_n|\psi_n\rangle$. The method is as follows [45]

(a) The average energy E_n is calculated from

$$E_n(a,b,\gamma) = \frac{\langle\psi_n(a,b)|H_r(\gamma)|\psi_n(a,b)\rangle}{\langle\psi_n(a,b)|\psi_n(a,b)\rangle} . \quad \text{(A-2)}$$

(b) E_n is minimized with respect to a and b

$$\left.\frac{\partial E_n}{\partial a}\right|_{(a_0,b_0)} = \left.\frac{\partial E_n}{\partial b}\right|_{(a_0,b_0)} = 0 . \quad \text{(A-3)}$$

(c) The upper bound of the energy level is given by

$$E_n = E_n(a_0,b_0,\gamma) . \quad \text{(A-4)}$$

The variational 1S, $2P_0$, and $2P_\pm$ wavefunctions used in eq. (A-2) are given in Table 3-2. The wavefunctions are such

that $\langle\psi_n(a,b)|\psi_n(a,b)\rangle = 1$.

In the following, $E_n(a_0,b_0,\gamma)$ will only be given since the calculations involved are elementary and very long. For each energy level, it was verified that E_n had the correct limiting behaviour

$$\lim_{(a_0,b_0,\gamma)\to(n,n,1)} E_n(a_0,b_0,\gamma) = -\frac{1}{n^2} . \qquad \text{(A-5)}$$

1. <u>1S STATE</u>

$$\gamma = 2\left(\sinh^{-1}\alpha - \frac{\alpha}{(1+\alpha^2)^{1/2}}\right)\left(\frac{\alpha}{(1+\alpha^2)^{3/2}} - \frac{\sinh^{-1}\alpha}{(1+\alpha^2)^2}\right)^{-1} , \qquad \text{(A-6)}$$

$$a = \frac{1}{3}\left(2 + \frac{\gamma}{1+\alpha^2}\right)\left(\frac{\sinh^{-1}\alpha}{\alpha}\right)^{-1} , \qquad \text{(A-7)}$$

$$E_{1S} = \frac{1}{3a^2}\left(2 + \frac{\gamma}{1+\alpha^2}\right) - \frac{2}{a}\,\frac{\sinh^{-1}\alpha}{\alpha} , \qquad \text{(A-8)}$$

where

$$\alpha^2 = \left(\frac{b}{a}\right)^2 - 1 . \qquad \text{(A-9)}$$

This system of equations agrees with those of Keyes [44] for an isotropic dielectric constant.

2. <u>$2P_0$ STATE</u>

$$\gamma = \frac{5a}{4}\,\frac{(1+\alpha^2)^{3/2}}{\alpha^2} - \frac{2}{3}(1+\alpha^2) - \frac{5a}{4}\,\frac{(1+\alpha^2)}{\alpha^2}\,\frac{\sinh^{-1}\alpha}{\alpha} , \qquad \text{(A-10)}$$

$$a = \frac{4}{15}\left[\frac{(1+\alpha^2)^{1/2}}{\alpha^2} - \frac{(1+\alpha^2)^{3/2}}{\alpha^4} - \frac{(1+\alpha^2)^{1/2}}{2\alpha^4} + \frac{\sinh^{-1}\alpha}{\alpha} \times \left[-\frac{1}{2\alpha^2} + \frac{3}{2}\frac{(1+\alpha^2)}{\alpha^4}\right]\right]^{-1}, \tag{A-11}$$

$$E^0_{2P} = \frac{1}{5a^2}\left(2 + \frac{3\gamma}{1+\alpha^2}\right) - \frac{3}{2a}\frac{(1+\alpha^2)^{1/2}}{\alpha^2} + \frac{3}{2a}\frac{\sinh^{-1}\alpha}{\alpha^3}. \tag{A-12}$$

3. <u>$2P_{\pm}$ STATE</u>

$$\gamma = -4(1+\alpha^2) - \frac{15}{8}a\frac{(1+\alpha^2)^{3/2}}{\alpha^2} + \frac{15a}{4}(1+\alpha^2) \times \frac{\sinh^{-1}\alpha}{\alpha} + \frac{15a}{8}(1+\alpha^2)\frac{\sinh^{-1}\alpha}{\alpha^3}, \tag{A-13}$$

$$a = \frac{16}{15} \times \left[\frac{(1+\alpha^2)^{1/2}}{4}(1/2 + (1+\alpha^2)) - \left[\frac{2(1+\alpha^2)-1/2}{\alpha^4}\right]\frac{\sinh^{-1}\alpha}{\alpha}\right]^{-1}, \tag{A-14}$$

$$E^{\pm}_{2P} = \frac{1}{5a^2}\left(4 + \frac{\gamma}{1+\alpha^2}\right) - \frac{3}{2a}\frac{\sinh^{-1}\alpha}{\alpha} + \frac{3}{4a}\frac{(1+\alpha^2)^{1/2}}{\alpha^2} - \frac{3}{4a}\frac{\sinh^{-1}\alpha}{\alpha^3}. \tag{A-15}$$

BIBLIOGRAPHY

1. R. Hilsch and R.W. Pohl, Z. Physik, 48, 384 (1928); 57, 145 (1929); 59, 812 (1930).

2. J. Frenkel, Phys. Rev., 37, 17 (1931); 37, 1276 (1931).

3. R.E. Peierls, Ann. Physik, [5], 13, 905 (1932).

4. J. Frenkel, Physik Z. Sowjetunion, 9, 158 (1936).

5. G.H. Wannier, Phys. Rev., 52, 191 (1937).

6. N.F. Mott, Trans. Faraday Soc., 34, 500 (1938).

7. J.R. Haynes, Phys. Rev. Lett., 4, 361 (1960).

8. E.E. Haller and W.L. Hansen, Phys. Rev. B, 21, 279 (1974).

9. M.O. Henry, E.C. Lightowlers, N. Killoran, D.J. Dunstan and B.C. Cavenett, J. Phys. C, 14, L255 (1981).

10. R.K. Crouch, J.B. Robertson and T.E. Gilmer, Jr., Phys. Rev. B, 5, 3111 (1972).

11. D.H. Martin and E. Puplett, Infrared Phys., 10, 105 (1969).

12. T. Timusk and F.K. Lin, Proc. of the 35th Symposium on Molecular Spectroscopy, Colombus, Ohio, 1980, p. 68.

13. D.H. Drew and A.J. Sievers, Appl. Opt., 8, 2067 (1969).

14. S.E. Whitcomb and J. Keene, Appl. Opt., 19, 197 (1980).

15. Y. Yamada, A. Mitsuishi and H. Yoshinaga, J. Opt. Soc. Am., 52, 17 (1962).

16. R.W. Scholes, M.Sc. thesis, McMaster University, 1983 (unpublished).

17. H. Navarro, Ph.D. thesis, McMaster University, 1979 (unpublished).

18. 1 kg = 9.81 Newtons. Also
$1\ kg/mm^2 = 9.81\ MPa,$
$= 98.1\ bar.$

19. A short description of the circuit is given by: R.P. Turner, Mosfet circuits guidebook - with 100 tested projects, Tab Books, 1975, p. 131.

20. J.T. Richards and R.M. Brick, J. Metals, May, 574 (1954).

21. CRC Handbook of Chemistry and Physics, 63rd edition 1982-1983, CRC Press, Inc., Florida.

22. E.M. Gershenzon, G.N. Gol'tsman and N.G. Ptitsina, Pis'ma Zh. Eksp. Teor. Fiz., 16, 228 (1972), [JETP Lett., 16, 161 (1972)].

23. V.S. Vavilov, N.V. Guzeev, V.A. Zayats, V.L. Kononenko, T.S. Mandel'shtam and V.N. Murzin, Pis'ma Zh. Eksp. Teor. Fiz., 17, 480 (1973), [JETP Lett., 17, 345 (1973)].

24. E.M. Gershenzon, G.N. Gol'tsman and N.G. Ptitsina, Pis'ma Zh. Eksp. Teor. Fiz., 18, 160 (1973), [JETP Lett., 18, 93 (1973)].

25. N.V. Guzeev, V.A. Zayats, V.L. Kononenko, T.S. Mandel'shtam and V.N. Murzin, Fiz. Tekh. Poluprovodn., 8, 1633 (1974), [Sov. Phys. Semicond., 8, 1061 (1975)].

26. E.M. Gershenzon, G.N. Gol'tsman and N.G. Ptitsina, Pis'ma Zh. Eksp. Teor. Fiz., 70, 224 (1976), [Sov. Phys.-JETP, 43, 116 (1976)].

27. M. Buchanan and T. Timusk, Proc. Int. Conf. Phys. Semicond., Rome (1976), p. 821.

28. V.I. Sidorov and Ya. E. Pokrovskii, Fiz. Tekh. Poluprovodn., 6, 2405 (1972), [Sov. Phys. Semicond., 6, 2015 (1973)].

29. A. Frova, G.A. Thomas, R.E. Miller and E.O. Kane, Phys. Rev. Lett., 34, 1572 (1975).

30. N.O. Lipari and M. Altarelli, Phys. Rev. B, 15, 4883 (1977).

31. M. Altarelli and N.O. Lipari, Phys. Rev. B, 15, 4898 (1977).

32. N.O. Lipari, M. Altarelli and E. Tosatti, Solid State Commun., 21, 979 (1977).

33. K. Muro and S. Narita, Proc. Int. Conf. Phys. Semicond., Rome (1976), p. 853.

34. M. Yamanaka, K. Muro and S. Narita, J. Phys. Soc. Japan, 44, 1222 (1978).

35. B.J. Feldman, H.-h. Chou and G.K. Wong, Solid State Commun., 24, 521 (1977); 26, 209 (1978).

36. R.L. Aggarwal, P. Fisher, V. Mourzine and A.K. Ramdas, Phys. Rev., 138, A882 (1965).

37. F. Herman, Proc. Inst. Radio Eng. Engrg., 43, 1703 (1955).

38. G. Dresselhaus, A.F. Kip and C. Kittel, Phys. Rev., 98, 368 (1955).

39. B.W. Levinger and D.R. Frankl, J. Phys. Chem. Solids, 20, 281 (1961).

40. I. Balslev, Phys. Rev., 143, 636 (1966).

41. a) J.C. Hensel and K. Suzuki, Phys. Rev. B, 9, 4219 (1974); b) S.M. Kelso, Phys. Rev. B, 25, 1116 (1982).

42. R.A. Faulkner, Phys. Rev., 184, 713 (1969).

43. W. Kohn and J.M. Luttinger, Phys. Rev., 98, 915 (1955).

44. R.W. Keyes, IBM J. Res. Develop., 5, 65 (1961).

45. The Raleigh-Ritz method is explained in standard textbook of Quantum Mechanics. See for example: A. Messiah, Quantum Mechanics, vol. 2, John Wiley and Sons, Inc., New York.

46. The absorption coefficient of a collection of atoms is derived in textbooks of Quantum Physics. See for example: A. Yariv, Quantum Electronics, 2nd ed., John Wiley and Sons, Inc., New York, 1975.

47. H.-h. Chou, J. Bajaj, G.K. Wong and B.J. Feldman, J. Lumin., 18/19, 573 (1979).

48. H.G. Zárate and T. Timusk, Can. J. Phys., 60, 1008 (1982).

49. The $3P_0$ and $3P_{\pm}$ energy levels were obtained by extrapolating Faulkner's calculation to a value of $\gamma^{1/3}$ = 1.0843. See ref. 42.

50. N. Killoran, D.J. Dunstan, M.O. Henry, E.C. Lightowlers and B.C. Cavenett, J. Phys. C, 15, 6067 (1982).

51. M.L.W. Thewalt, S.P. Watkins, U.O. Ziemelis, E.C. Lightowlers and M.O. Henry, Solid State Commun., 44, 573 (1982).

52. J.J. Hopfield, D.G. Thomas and R.T. Lynch, Phys. Rev. Lett., 17, 312 (1966).

53. E. Cohen and M.D. Sturge, Phys. Rev. B, 15, 1039 (1977).

54. Several papers have been published on this topic. See N.O. Lipari, A. Baldereschi and M.L.W. Thewalt, Solid State Commun., 33, 277 (1980), and references therein.

55. See for example, J.C. Hensel, T.G. Phillips and G.A. Thomas, Solid State Physics, vol. 32, ed. H. Ehrenreich, F. Seitz and D. Turnbull, Academic Press, 1977.

56. A. Onton, P. Fisher and A.K. Ramdas, Phys. Rev., 163, 686 (1967).

57. 43 meV was obtained from the binding energy of boron acceptor [56] minus 3 meV.

58. N.O. Lipari and A. Baldereschi, Solid State Commun., 25, 665 (1978).

59. M.L.W. Thewalt, Private communication; see also D. Labrie, T. Timusk and M.L.W. Thewalt, Phys. Rev.

Lett., 52, 81 (1984).

60. M.L.W. Thewalt, Solid State Commun., 23, 733 (1977).

61. G.B. Wright and A. Mooradian, Phys. Rev. Lett., 18, 608 (1967).

62. T. Timusk, Phys. Rev. B, 13, 3511 (1976).

63. J.B. Mock, G.A.Thomas and M. Combescot, Solid State Commun., 25, 279 (1978).

64. P.L. Gourley and J.P. Wolfe, Phys. Rev. B, 25, 6338 (1982).

65. G.A. Thomas and T.M. Rice, Solid State Commun., 23, 359 (1977).

66. M. Combescot and P. Nozières, Solid State Commun., 10, 301 (1972).

67. J.H. Rose, H.B. Shore and T.M. Rice, Phys. Rev. B, 17, 752 (1978).

68. H.G. Zárate and T. Timusk, Phys. Rev. B, 19, 5223 (1979).

69. The computer program was written by H.G. Zárate, modified by T. Timusk and the author.

70. Y.E. Pokrovskii and K.I. Svistunova, Fiz. Tverd. Tela., 13, 1485 (1971), [Sov. Phys.-Solid State, 13, 1241 (1971)]; R.W. Martin, Phys. Status Solidi B, 61, 223 (1974); B.J. Feldman, Phys. Rev. Lett., 33, 359 (1974).

71. S. Krauzewicz, M.Sc. thesis, McMaster University, 1981 (unpublished).

72. For a review, see T.M. Rice, Solid State Physics, vol. 32, ed. H. Ehrenreich, F. Seitz and D. Turnbull, Academic Press, Inc., New York; J.C. Hensel, T.G. Phillips and G.A. Thomas, ibid.

73. We have used the same parameters as G.A. Thomas and T.M. Rice, [65].

74. The optical effective mass of excitons was used in the expression given by Timusk, [62].

75. The free carrier concentration was estimated by using eq. (5-10) and with the absorption spectrum at 7.3K. The Drude damping constant was obtained from Brooks-Herring formula given by eq. 5 of P.P. Debye and E.M. Conwell, Phys. Rev., 93, 693 (1954).

76. J.R. Meyer and M. Glicksman, Phys. Rev. B, 17, 3227 (1978). The Drude damping constant was obtained by assuming $\tau_{e-ph} = \tau_{h-ph}$. The units of Γ are such that 1 meV = 1.52×10^{12} ra/sec.

77. H. Kawamura, H. Saji, M. Fukai, K. Sekido and I. Imai, J. Phys. Soc. Jpn., 19, 288 (1964).

78. L.J. Schowalter, F.M. Steranka, M.B. Salamon and J.P. Wolfe, Phys. Rev. B, 29, 2970 (1984), and references therein; G.A. Thomas, J.B. Mock and M. Capizzi, Phys. Rev. B, 18, 4250 (1978), and references therein.